



Systemic dysfunction and plasticity of the immune macroenvironment in cancer models

Breanna M. Allen^{1,2,6}, Kamir J. Hiam^{1,2,6}, Cassandra E. Burnett^{1,2}, Anthony Venida^{1,3}, Rachel DeBarge^{1,2}, Iliana Tenvooren², Diana M. Marquez^{1,2}, Nam Woo Cho^{2,4}, Yaron Carmi^{1,5} and Matthew H. Spitzer^{1,2}✉

Understanding of the factors governing immune responses in cancer remains incomplete, limiting patient benefit. In this study, we used mass cytometry to define the systemic immune landscape in response to tumor development across five tissues in eight mouse tumor models. Systemic immunity was dramatically altered across models and time, with consistent findings in the peripheral blood of patients with breast cancer. Changes in peripheral tissues differed from those in the tumor microenvironment. Mice with tumor-experienced immune systems mounted damped responses to orthogonal challenges, including reduced T cell activation during viral or bacterial infection. Antigen-presenting cells (APCs) mounted weaker responses in this context, whereas promoting APC activation rescued T cell activity. Systemic immune changes were reversed with surgical tumor resection, and many were prevented by interleukin-1 or granulocyte colony-stimulating factor blockade, revealing remarkable plasticity in the systemic immune state. These results demonstrate that tumor development dynamically reshapes the composition and function of the immune macroenvironment.

Immunotherapy has rapidly expanded the toolkit against cancer, but a broader understanding of factors governing immune responses in cancer is required to extend clinical efficacy to all patients. Intratumoral CD8 T cells have been the main focus of cancer immunotherapies, but recent studies have demonstrated that cytotoxic T cells within the tumor microenvironment (TME) are irreversibly dysfunctional¹. Several studies have shown that a systemic anti-tumor immune response is essential for immunotherapeutic efficacy^{2–9}. However, a comprehensive definition of how cancer development affects the systemic immune state is lacking.

Several lines of evidence suggest that systemic immune perturbations occur with cancer. Peripheral granulocytic and monocytic expansion and impaired differentiation accompany tumor progression^{10–12} along with a reduction in conventional dendritic cells¹³. Systemic effects on lymphocytes remain poorly understood. Most studies have explored anti-tumor immune responses at a single, static time point, leaving the dynamicity of the immune system during cancer development an open question. Prior immune experiences can affect responses to new stimuli by shifting basal cytokine levels, innate immune activation states and cellular composition^{14–16}. Although many immunotherapies and vaccines seek to elicit new immune responses in patients with cancer, it remains uncertain how tumor burden affects these processes. It is also unclear whether there are lasting immune effects after successful primary tumor clearance, although studies have associated tumor resection with a reduction in myeloid-derived suppressor cells^{17,18}. Defining the functional capacity and stability of the tumor-experienced immune macroenvironment is critical for improving immunotherapies.

In this study, we used high-content single-cell analysis and corresponding analytical methods to characterize the systemic immune

landscape across eight commonly used mouse tumor models. These data, which are publicly available, provide a rich resource. Although each tumor has unique immunologic consequences, we found that three distinct breast cancer models converged on similar systemic changes. Tumors drove dynamic shifts in the organization and functional capacity of immune cells across the organism, culminating in attenuated responses to new immune challenges, and tumor resection was sufficient to revert the systemic immune landscape. These findings have implications for how and when we apply immunomodulatory agents in cancer, emphasizing the importance of strategies that are informed by preexisting alterations in the immune macroenvironment.

Results

Systemic immune organization is altered across multiple tumor types. We began by examining the TME across several common mouse tumor models, including genetically engineered and transplantable syngeneic models across different mouse strains with different mutational loads, metastatic potential, variability and latency in tumor growth^{19–22}. We characterized well-established but pre-terminal tumor stages to reflect the patient populations most often treated with immunotherapies, but also to avoid the confounding effect of end-of-life processes. We used mass cytometry to quantify the abundance and activity state of immune cell subsets in the tumor as well as the blood, spleen, bone marrow and tumor-draining lymph nodes (Supplementary Table 1 and Extended Data Fig. 1).

The immune composition of the TME was distinct between models, varying in the degree of immune infiltration and diversity (Fig. 1a and Extended Data Fig. 2a). The predominant immune

¹Graduate Program in Biomedical Sciences, University of California, San Francisco, San Francisco, CA, USA. ²Departments of Otolaryngology and Microbiology & Immunology, Helen Diller Family Comprehensive Cancer Center, Parker Institute for Cancer Immunotherapy, Chan Zuckerberg Biohub, University of California, San Francisco, San Francisco, CA, USA. ³Department of Anatomy, University of California San Francisco, San Francisco, CA, USA.

⁴Department of Radiation Oncology, University of California San Francisco, San Francisco, CA, USA. ⁵Department of Pathology, Sackler School of Medicine, Tel Aviv University, Tel Aviv, Israel. ⁶These authors contributed equally: Breanna M. Allen, Kamir J. Hiam. ✉e-mail: matthew.spitzer@ucsf.edu

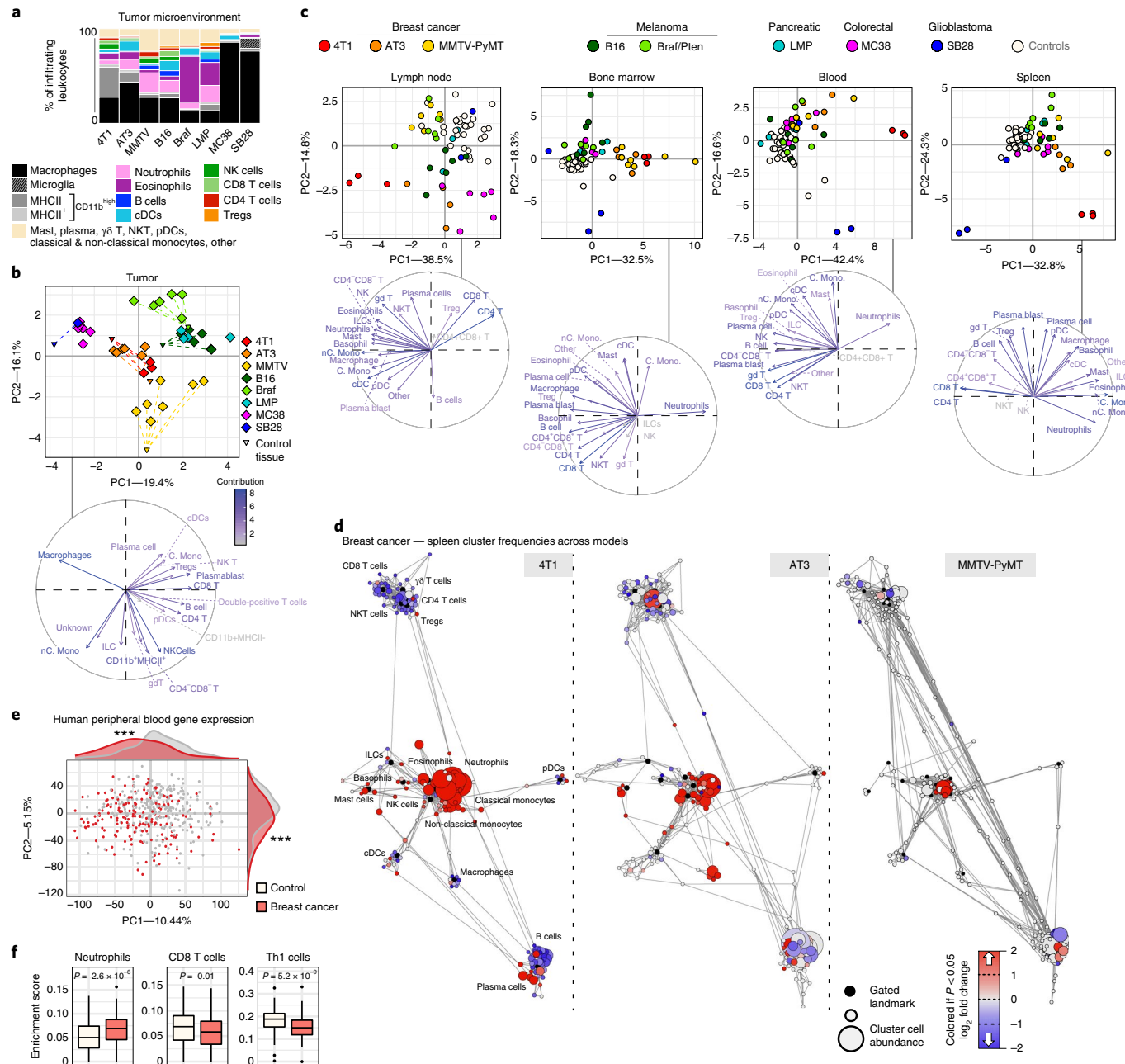


Fig. 1 | The systemic immune landscape is remodeled across tumor models. **a**, Composition of tumor immune infiltrates across late-stage mouse models, identified by manual gating ($n=3$ independent animals for 4T1; $n=6$ AT3; $n=7$ MMTV-PyMT; $n=6$ B16; $n=6$ Braf/Pten; $n=4$ LMP; $n=6$ MC38; $n=1$ SB28; $n=30$ controls). **b,c**, PCA and corresponding vector plot of individual contributions for the tumor-infiltrating immune frequencies (**b**) and the \log_2 fold change of immune frequencies for the tumor-draining lymph node, bone marrow, blood and spleen (**c**) identified manually ($n=3$ for SB28, otherwise as in **a**). **d**, Scaffold maps of spleen immune frequencies in breast tumor models (4T1, AT3 and MMTV-PyMT). Black nodes represent canonical cell populations identified manually. Other nodes reflect unsupervised clustering of leukocytes. Nodes are arranged by similarity using a force-directed graphing algorithm (see Methods). Red denotes populations significantly higher in frequency in tumor-burdened animals compared to controls; blue denotes significantly lower frequency. For significant nodes ($q < 0.05$ by significance analysis of microarrays), the degree of coloring reflects the \log_2 fold change (n as in **a**). **e,f**, PCA (**e**) and significant immune changes by cellular enrichment analysis (**f**) from human whole blood gene expression, comparing patients with breast cancer ($n=173$) and matched controls ($n=281$). *** $P < 0.001$ by two-sided Wilcoxon rank-sum test with Benjamini-Hochberg correction. Box plots: center line, median; box limits, upper and lower quartiles; whiskers, $1.58 \times$ interquartile range / \sqrt{n} ; points, outliers.

cell types were tumor-associated macrophages and other CD11b^{high} myeloid subsets, particularly in the transplantable MC38 colorectal cancer and SB28 glioblastoma models, with relatively fewer adaptive immune cells as reported in many human tumors²³. Both transplantable LMP pancreatic cancer and genetically induced Braf/Pten

melanoma models showed extensive eosinophil infiltration. B16-F10 syngeneic melanoma and three models of breast cancer (transplantable cell lines 4T1 and AT3 and autochthonous MMTV-PyMT) showed less relative abundance but greater diversity in local immune cells, including B, T and natural killer (NK) cell infiltration (Fig. 1a

and Extended Data Fig. 2a). Unique immune profiles were apparent across tumor types (Fig. 1b and Extended Data Fig. 2g).

We next asked whether these tumor models also resulted in altered systemic immune states. The immune compositions of the tumor-draining lymph node, bone marrow, blood and spleen were indeed altered, with nuance in the extent of alteration and immune cell types affected (Fig. 1c and Extended Data Fig. 2g). There was striking concordance among different models of the same tumor type (breast cancer and melanoma), shifting together across principal components. Surprisingly, SB28 glioblastoma extensively altered systemic immunity despite localization in the brain. Reporter protein expression was not responsible for systemic immune remodeling, as both the AT3 parental cell line and a derivative expressing green fluorescent protein (GFP) and luciferase exhibited strongly correlated systemic alterations (Extended Data Fig. 2h, $r=0.9$, $P=2.2 \times 10^{-16}$). Systemic alterations also occurred in mice both with and without metastases (Extended Data Fig. 3a–e) and were tightly correlated with primary tumor size in the MMTV-PyMT model ($r=0.8527$, $P<0.0001$). Although most systemic immune remodeling could be explained by primary tumor size (78.4%), the residual values were correlated with both lung and lymph node metastases ($r=0.5794$, $P=0.0207$ for lung and $r=0.5882$, $P=0.0185$ for lymph node). Compositional alterations in these peripheral sites did not correspond with the local immune infiltrate. Thus, tumor burden drives distinct changes in peripheral immune organization, dependent on the identity of the tumor.

We next performed Statistical Scaffold Analysis^{2,24} to interrogate the effect of tumor burden in a more detailed manner, focusing initially on the spleen as a secondary lymphoid organ distal from the tumor (Fig. 1d, Extended Data Fig. 2b–f and Methods). All models exhibited expansions in the splenic myeloid compartment, which was dominant in some, such as the three breast cancer models (Fig. 1d and Supplementary Table 2), but less dramatic in others, such as the two melanoma models (Extended Data Fig. 2e,f). Splenic remodeling in breast cancer was specifically characterized by increases in frequencies of neutrophils, eosinophils and monocytes and reductions in B and T cells (Fig. 1d). Consistency was observed across breast cancer models, which spanned three mouse strain backgrounds (BALB/c for 4T1, C57BL/6 for AT3 and FVB/N for MMTV-PyMT), orthotopic and autochthonous models and a range of metastatic potential (AT3—weakly metastatic, MMTV-PyMT—moderately metastatic and 4T1—highly metastatic). Consistency despite model differences argues for a tumor and/or site-specific bias in systemic immune responses. Gene expression analysis of whole blood from untreated patients with breast cancer and matched controls from the Norwegian Women and Cancer Study also demonstrated a marked shift in the immune state (PC1 Wilcoxon rank-sum $P=5.0 \times 10^{-12}$, PC2 $P=1.6 \times 10^{-6}$) (Fig. 1e). Cellular enrichment analysis demonstrated increased neutrophils and decreased Th1 and CD8 T cells (Fig. 1f). Altogether, these data suggest that tumor burden broadly disrupts immune macroenvironments, providing context to inform therapeutic manipulations designed to activate local versus systemic responses.

Tumor growth drives nonlinear changes in immune cell frequencies over time. Tumors develop gradually, but tumors are sampled at one developmental point in the clinic to provide prognostic information related to the immune response. We explored the dynamics of global immune remodeling during breast tumor growth, beginning with the predictable orthotopic 4T1 model before confirming results in an unrelated spontaneous model (MMTV-PyMT). Absolute cell counts of tumor-infiltrating leukocytes positively correlated with tumor size, supporting a progressive immune response (Extended Data Fig. 3f, $r=0.6$, $P=0.0256$). Absolute spleen cell counts also increased, but cell frequencies as a percent of total leukocytes were

similar to absolute numbers per milligram of spleen (Extended Data Fig. 3g). Deep profiling of both the tumor and splenic immune compositions by mass cytometry revealed nonparametric correlations in individual cluster frequencies with time (Fig. 2a,b), demonstrating at the single-cell level that immune changes are indeed progressive. Principal component analysis (PCA) of immune cell frequencies showed progressive changes across tissues over tumor growth in both 4T1 (Fig. 2c,d) and MMTV-PyMT tumors (Extended Data Fig. 3h). Notably, the immune profile within the TME remained distinct from those observed in peripheral sites. The draining lymph node immune composition was unique, whereas the spleen, blood and bone marrow were more coordinated. Neutrophil expansion in the spleen and bone marrow, culminating in elevated circulation in blood but lack of accumulation within the lymph node or tumor, is one feature contributing to these unique profiles (Fig. 2d).

Progressive systemic immune responses to tumor burden were not strictly linear. The magnitude of change was nonuniform between each timepoint as evident by the PCA (Fig. 2c and Extended Data Fig. 3h). Although some population changes were relatively continuous, such as increasing neutrophils or decreasing CD4⁺ T cells, many others were dynamic, such as CD8⁺ T cells and regulatory T cells (Tregs), which reciprocally expanded and contracted at distinct times in the tumor and draining lymph node (Fig. 2d). In the spleen, myeloid expansion began by day 7 and continued to day 14, preceding the progressive decline in the T and B cells that began by day 14 (Extended Data Fig. 3i). The lymph node also changed most dramatically by day 14 (Extended Data Fig. 4a), whereas changes in blood were more continuous (Extended Data Fig. 4b). The bone marrow and tumor contained less mature and clearly defined cell types, with many more intercluster connections and individualized patterns of change over tumor growth (Extended Data Fig. 4c,d). These data demonstrate that the tumor immune response is a highly dynamic process.

Immune cell states are dynamically altered across immune organs with tumor growth. To understand the extent of systemic effects on T cells, we leveraged unsupervised cell clustering to identify changes in T cell subsets, cell states and potential cross-organ coordination of responses during tumor growth. Indeed, the T cell compartment was dramatically reorganized over both 4T1 and MMTV-PyMT tumor development (Fig. 3a and Extended Data Fig. 5a,b). Tissues contained both unique and shared T cell subsets shifting with tumor growth (Fig. 3b,c and Extended Data Fig. 5c–e). Blood and spleen profiles were more similar, dominated by CD4⁺ T cells. In contrast, the tumor T cell pool had more shared subsets with the bone marrow, including an increasing double-negative population and a decreasing natural killer T (NKT) cell population (Fig. 3c).

Demonstrating the breadth of immune reorganization in cancer, all T cell clusters changed in abundance across multiple tissues between early and late disease timepoints (Fig. 3d). Of particular interest, tumor-infiltrating CD103⁺ Tregs, described as potent suppressors of effector T cells²⁵, were abundant at day 7 but decreased with tumor progression (Fig. 3e). This Treg subset expanded in the draining lymph node, suggesting that distal suppressive mechanisms might support local changes to maintain a tumor-promoting systemic state. Anti-correlated changes extended to conventional CD4 T cells, where CD44⁺CD90^{high}-activated CD4 T cells decreased in the tumor but expanded in the lymph node (Fig. 3f). The spleen showed the greatest change in CD44⁺CD27⁺ memory CD4⁺ T cells, which decreased with disease progression (Fig. 3g). The blood showed increases of activated CD44⁺CD4⁺ T cells expressing the CD31 adhesion receptor, which can promote T cell survival in settings of inflammation (Fig. 3h)²⁶. CD44⁺CD8⁺ T cells expanding in the lymph node expressed Ly6C (Fig. 3j), which can support lymph node homing of central memory T cells²⁷. CD8⁺ T cells generally

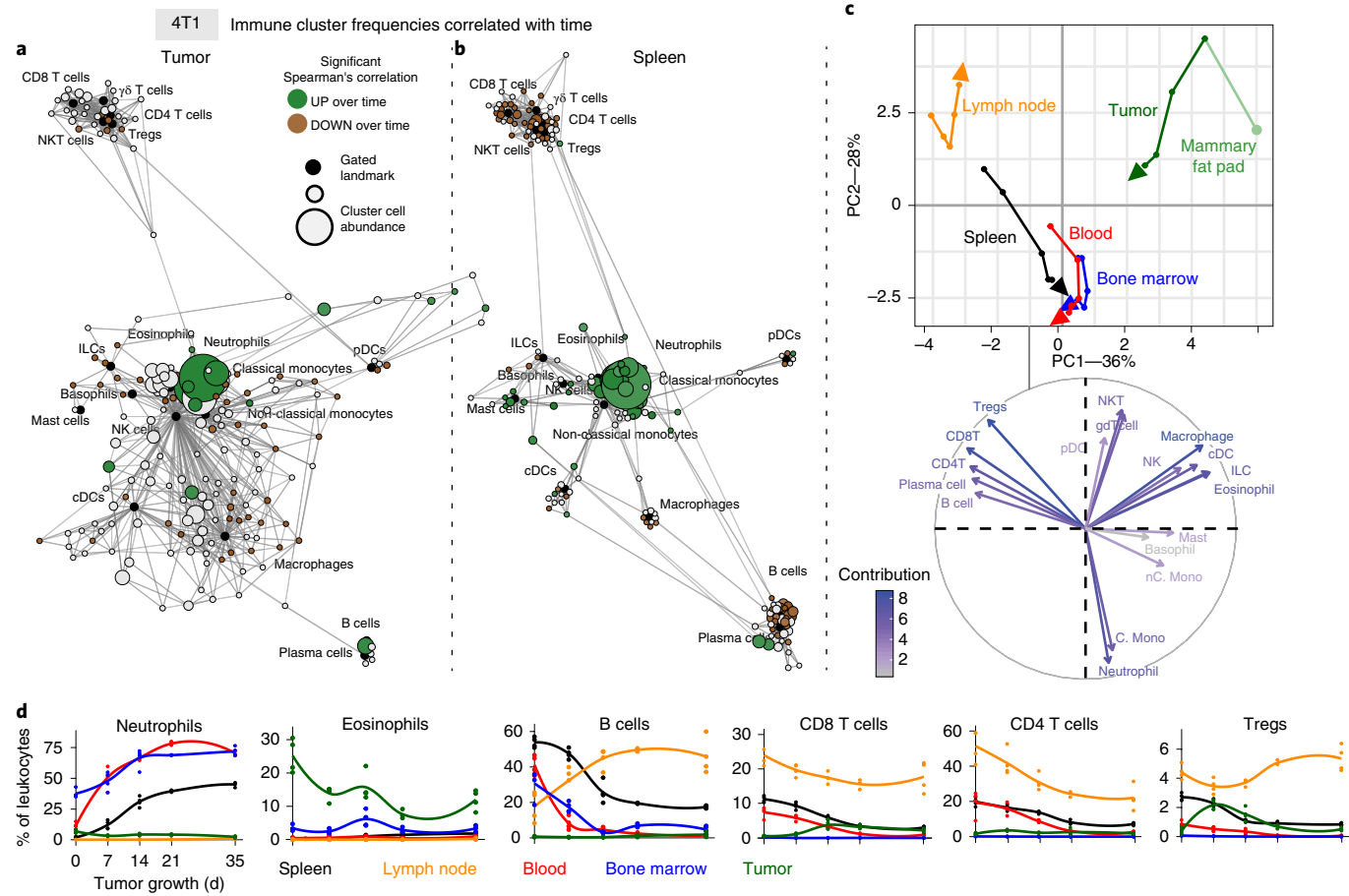


Fig. 2 | The systemic immune landscape is remodeled progressively with tumor development. **a,b**, Scaffold maps of 4T1 tumor (**a**) and spleen (**b**) cell frequencies colored by significant Spearman's correlation with time (across day 0, 7, 14, 21 and 35), $P < 0.05$ by two-sided *t*-test with Benjamini-Hochberg correction. Green denotes positive correlation; brown denotes negative correlation. **c**, PCA and corresponding vector plot of contributions for immune cell frequencies from each immune tissue over 4T1 breast tumor growth. Vectors designate progression from control day 0 (first point) to day 7, 14, 21 and 35 (last point, arrowhead). **d**, Curves of mean cell frequencies across time from a subset of immune cell types contributing to **c**, colored by tissue corresponding with **c**. All panels are from one experiment. $n=3$ independent animals for day 21 and $n=4$ for all other timepoints.

expanded in the tumor, but the most dominant cluster expressed high levels of PD-1 and CD69 previously associated with T cell dysfunction (Fig. 3*i*)^{28,29}. To explore the extent of dysfunction, we interrogated intratumoral and splenic T cells for their expression of CD101 and CD38, two markers recently identified as evidence of permanent T cell dysfunction¹. Late-stage tumor burden led to accumulation of CD38⁺CD101⁺CD8⁺ T cells in the tumor as expected; however, this phenotype did not emerge in the spleen (Fig. 3*k*), suggesting that CD8⁺ T cells are altered differently in the TME and periphery. Similar changes in T cell composition were observed in the MMTV-PyMT model (Extended Data Fig. 5c–h).

A similar pan-organ clustering analysis for the mononuclear phagocyte subsets, including macrophages and dendritic cells (Extended Data Fig. 6), revealed correlated and anti-correlated systemic changes in cell states with tumor progression. As expected, the tumor-infiltrating subsets were distinct from peripheral subsets and expressed high levels of PD-L1.

We specifically interrogated protein expression dynamics of PD-1 and PD-L1, the most commonly manipulated immune checkpoints by cancer immunotherapies to facilitate T cell responses³⁰. Although expression of these molecules is used clinically for patient stratification, it remains unclear whether they are expressed consistently or modulated dynamically over time. We indeed found dynamic PD-1 and PD-L1 expression on infiltrating immune cells

(CD45⁺) and nonimmune cells (CD45[−]CD31[−]) in the TME and in the periphery of both 4T1 and AT3 breast cancer models (Extended Data Fig. 7a–c). In fact, although the overall amount of PD-L1 expression was significantly less in the blood than in the tumor, median leukocyte signal intensity was positively correlated between these tissues (Extended Data Fig. 7d, $r=0.7487$, $P=0.001$). Both PD-1 and PD-L1 were promiscuously expressed across immune cell types, particularly within the TME (Extended Data Fig. 7e). The most prominent cells expressing PD-L1 in the periphery were non-classical monocytes³¹ and classical dendritic cells (cDCs), whereas PD-1 was abundantly expressed on T cells, neutrophils and eosinophils. Dynamicity in PD-1 and PD-L1 expression suggests the potential for differential sensitivity to checkpoint blockade over the course of tumor development.

Changes in cellular proliferation or death rates are potential mechanisms contributing to immune composition alterations. We discovered that immune proliferation fluctuated systemically in a pattern unique to each site but was coordinated across all immune subsets within that site (Extended Data Fig. 8a–d). Changes in Ki67 and cleaved caspase-3 expression corresponded poorly with clusters that were increasing or decreasing in frequency in the spleen (Extended Data Fig. 8e). Thus, although tumor burden systemically alters proliferation and death, these processes alone likely do not account for the systemic immune alterations observed.

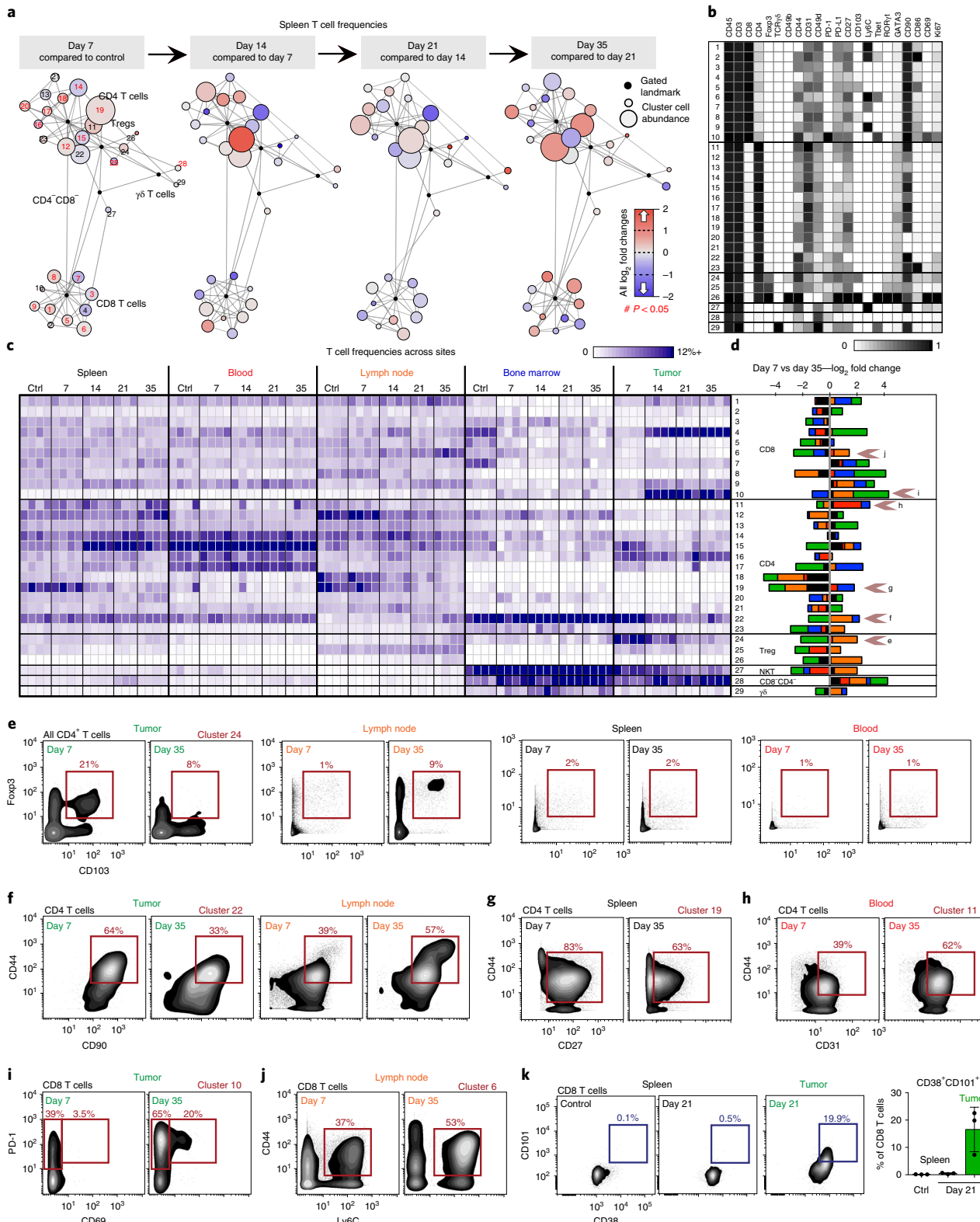


Fig. 3 | Tumor burden progressively changes the systemic T cell composition. **a-d**, CD3⁺CD11b⁻ leukocytes from all tissues from healthy and 4T1 tumor-burdened animals at progressive timepoints. **a**, Scaffold maps of the T cell cluster frequencies in the spleen at each disease stage, all colored by \log_2 fold change in frequency. Clusters with significant changes over time are highlighted in red in the first map, $q < 0.05$ by multiclass significance analysis of microarrays. **b**, Heat map of the protein expression defining each T cell cluster, column normalized to each protein's maximum positive expression. **c**, Heat map of each T cell cluster frequency, by row, in each site and across the individual 3–4 animals per timepoint. **d**, Stacked bar plot of the \log_2 fold change in cluster frequency between early (day 7) and late (day 35) disease stage, colored by tissue. **e-j**, Representative scatter plots of key proteins defining T cell clusters that change in frequency in the designated tissues between early and late disease stage for Tregs (**e**), CD4 T cells (**f-h**) and CD8 T cells (**i-j**). **k**, Representative scatter plots and quantification of CD101⁺CD38⁺ dysfunctional CD8 T cells in the spleen and tumor of healthy or day 21 tumor-burdened animals. All panels are from one experiment. $n=3$ independent animals for day 21 and $n=4$ for all other timepoints. Bar plot: center, mean; whiskers, s.d.

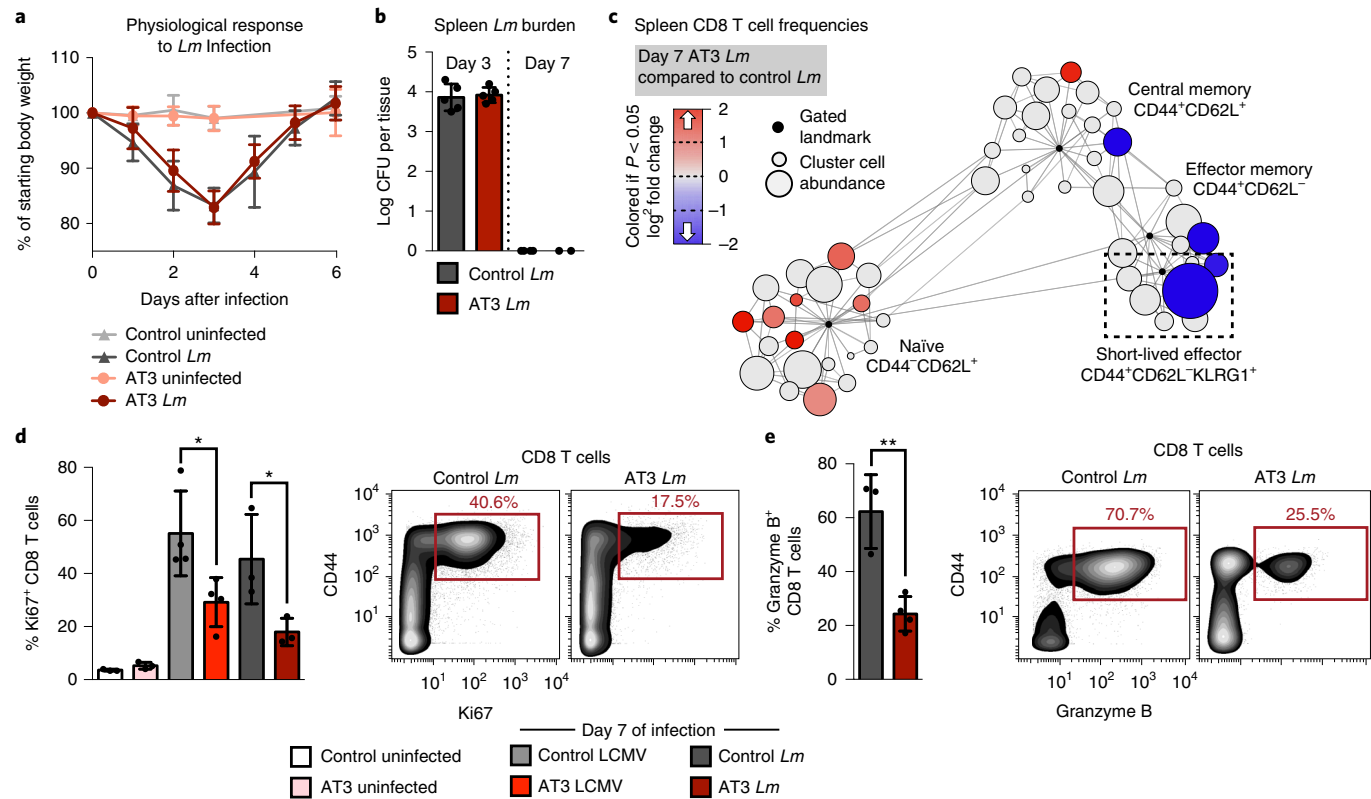


Fig. 4 | Tumor burden leads to impaired T cell responses to secondary infection. **a,b**, Fold change in body weight after *Lm* infection ($n=11$ independent animals for control groups and $n=9$ for AT3 groups) (**a**) and quantification of *Lm* bacterial burden (**b**) in control and AT3 tumor-burdened animals ($n=5$ for day 3 groups, $n=4$ for control day 8 and $n=2$ for AT3 day 8). **c**, Scaffold map of CD8 T cell frequencies in the spleen in AT3 tumor-burdened mice after 7 d of *Lm* infection, colored by fold change in frequency compared to infected control mice ($n=3$ uninfected, $n=3$ *Lm* infected), $q < 0.05$ by significance analysis of microarrays. **d,e**, Quantification and representative scatter plots of splenic CD8⁺ T cell proliferation (**d**) and granzyme B production (**e**) in response to LCMV Armstrong or *Lm* in healthy or AT3 tumor-burdened animals ($n=3$ uninfected, $n=4$ LCMV and $n=3$ *Lm* infected). For all bar plots, * $P < 0.05$ and ** $P < 0.01$ by two-sided t-test; center, mean; whiskers, s.d.

De novo T cell responses are impaired by preexisting malignancy. Having established that tumor development drives an altered immune macroenvironment, we next examined whether immune responses to new challenges were affected. Type 1 immune responses are associated with strong cellular immunity and are generally thought to provide optimal anti-tumor immunity. To understand how type 1 immune responses might take place in the context of cancer, we challenged healthy or AT3 tumor-bearing mice with two well-described pathogens that induce potent type 1 immunity, lymphocytic choriomeningitis virus (LCMV) and *Listeria monocytogenes* (*Lm*)^{32,33}. Tumor-burdened mice still cleared the pathogens from the spleen (Fig. 4a,b), consistent with the lack of complete immunosuppression in patients with solid tumors. However, the cellular immune response to infection was dramatically altered. The differentiation of effector CD8 T cells, the magnitude of CD8⁺ T cell proliferation and expression of the cytolytic mediator granzyme B were all significantly impaired in tumor-bearing mice after infection (Fig. 4c–e and Extended Data Fig. 9a). These results demonstrate an unappreciated impairment of new cellular immune responses in the context of cancer.

We previously found that CD8⁺ T cells with markers of terminal dysfunction were observed only in the TME and not in the spleen (Fig. 3k). Consistent with this hypothesis, splenic CD8⁺ T cells harvested from either control or tumor-burdened animals were equally capable of producing the key effector cytokines interferon (IFN)- γ , tumor necrosis factor (TNF)- α and interleukin (IL)-2 in vitro (Extended Data Fig. 9b). To test their functionality after infection, CD8⁺ T cells from OT-I transgenic

mice expressing a T cell receptor specific for ovalbumin (SIINFEKL) were isolated from control or tumor-bearing mice and transferred into recipient mice, which were infected with *Lm*-expressing ovalbumin (*Lm*-OVA). AT3 tumors still drove systemic changes in TCR transgenic mice (Extended Data Fig. 9c). OT-I CD8⁺ T cells from control and tumor-bearing mice proliferated equivalently in control recipients at day 7 after infection, the peak of the CD8 T cell response^{32–34} (Fig. 5a). However, when OT-I T cells were transferred into tumor-bearing recipients before infection, they expanded poorly, failed to induce T-bet expression associated with differentiation into effector cells and expressed higher levels of PD-1 (Fig. 5b). Similar results were also observed when polyclonal CD8 T cells from control or tumor-burdened mice were competitively transferred (Fig. 5c). We found that antigen-specific central memory, effector memory and short-lived effector CD8⁺ T cells were less abundant in tumor-bearing mice at day 10 as well, suggesting that defects extend beyond peak proliferation and represent a fundamental impairment of de novo CD8⁺ T cell responses (Fig. 5d). Together, these results demonstrate that cell extrinsic mechanisms suppress systemic T cell function in the tumor context.

Because tumor-experienced CD8⁺ T cells in the periphery were not dysfunctional, we hypothesized that impaired APC activity earlier during infection contributes to decreased peripheral CD8⁺ T cell activation. Dendritic cells (DCs) play a key role in orchestrating CD8⁺ T cell responses to *Lm*³⁵, and evidence suggests that circulating DCs in patients with breast cancer have reduced antigen presentation capacity³⁶. Therefore, we quantified co-stimulatory molecule

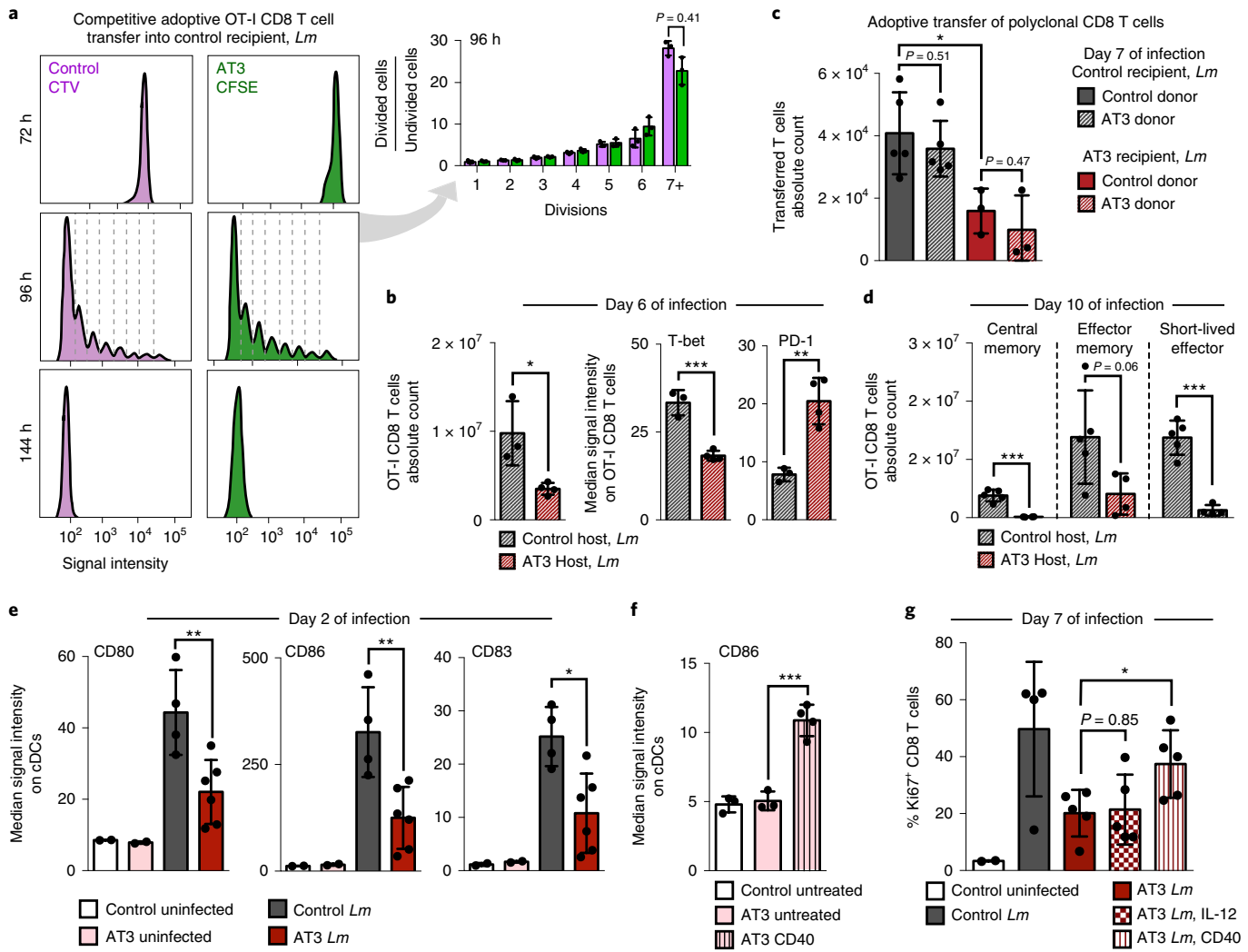
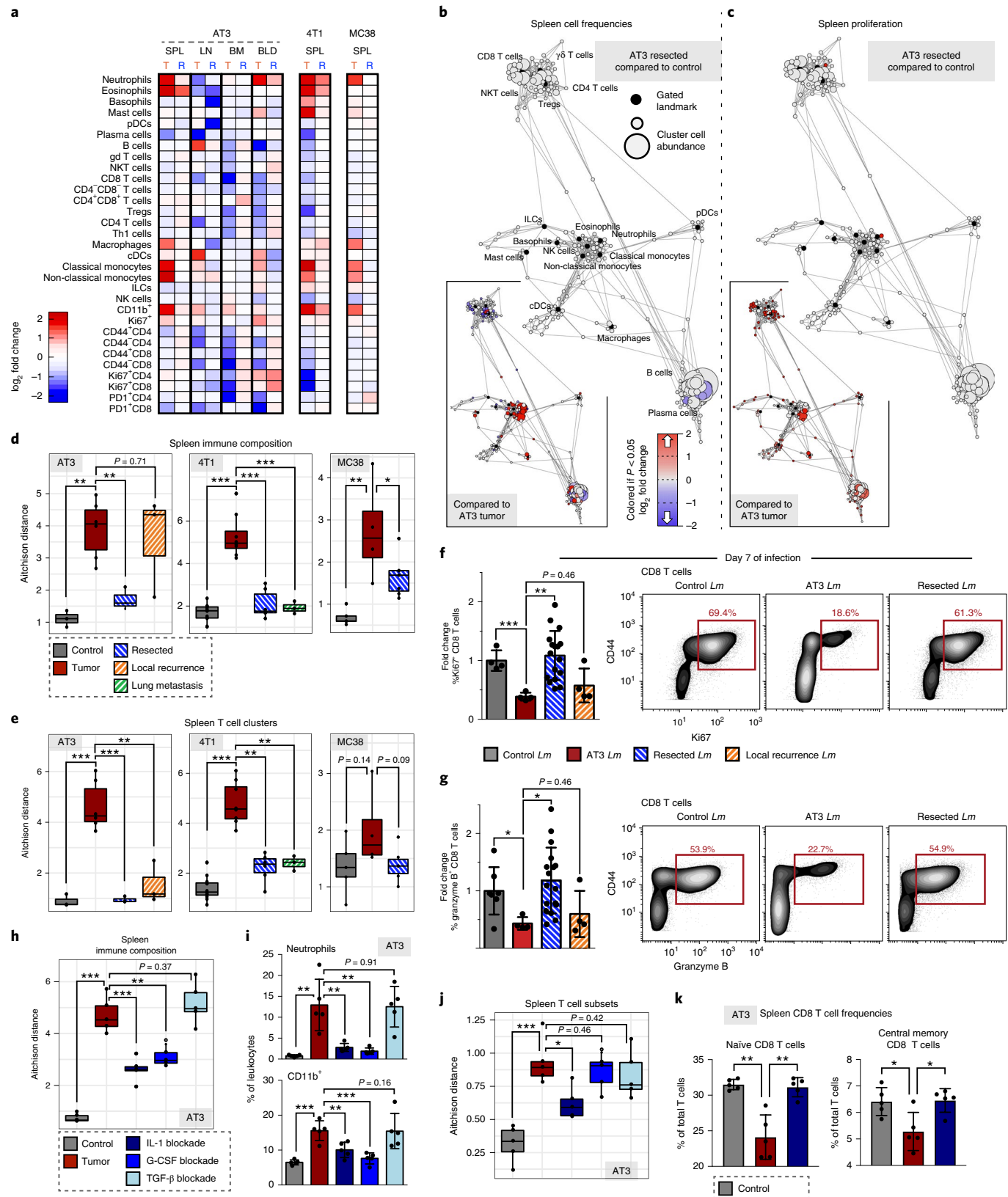


Fig. 5 | Tumor burden attenuates dendritic cell activation during secondary infection. **a**, OT-I T cell proliferation from control or tumor-burdened animals transferred into control recipients and analyzed at 72, 96 and 144 h after *Lm*-OVA infection ($n=3$ independent animals per group). Quantification of 96 h. **b**, Transferred OT-I T cell counts and median signal intensity of T-bet and PD-1 at day 6 of *Lm*-OVA infection ($n=3$ for control and $n=4$ for AT3 hosts). **c**, Competitively transferred polyclonal CD8 T cell counts from congenic (CD45.1⁺ AT3 tumor-burdened or CD45.1⁺CD45.2⁺ control) donors into CD45.2 control ($n=5$) or AT3 tumor-burdened recipients ($n=4$), after 7 d of *Lm* infection. **d**, CD8⁺ T cell subtype counts from transferred CD45.1⁺ OT-I T cells at day 10 of *Lm*-OVA infection ($n=5$ for control and $n=4$ for AT3 hosts). **e**, Median signal intensity of CD80, CD86 and CD83 on splenic cDCs from healthy ($n=4$) or AT3 tumor-burdened (day 28, $n=6$) mice at day 2 of *Lm*-OVA infection ($n=2$ for uninfected groups). **f**, Median signal intensity of CD86 on splenic cDCs from untreated ($n=3$) or CD40-treated ($n=4$) AT3 tumor-burdened (day 21) mice. **g**, Quantification of splenic CD8⁺ T cell proliferation in healthy versus untreated, IL-12p70-treated or anti-CD40-treated AT3 tumor-burdened animals at day 7 of *Lm*-OVA infection ($n=2$ control uninfected, $n=4$ control *Lm* and $n=5$ for AT3 groups). For all bar plots, * $P<0.05$, ** $P<0.01$ and *** $P<0.001$ by two-sided t-test; center, mean; whiskers, s.d.

expression on splenic DCs 2 d after infection. DCs from AT3 tumor-bearing animals expressed lower levels of key co-stimulatory molecules CD80 and CD86 and the activation marker CD83 when compared to tumor-free controls (Fig. 5e and Extended Data Fig. 9d). DCs from tumor-bearing mice also exhibited suboptimal activation at day 7 of infection, expressing lower levels of CD80, the adhesion molecule CD54 (ICAM-1) and PD-L1 (Extended Data Fig. 9e). This result suggests that the PD-1/PD-L1 axis does not cause the T cell response impairment and indicates that alternative strategies are likely required to induce new systemic T cell activity. We therefore sought to pharmacologically boost APC activation as a plausible strategy for achieving this goal. Anti-CD40 treatment drives potent and systemic APC activation as shown by elevated CD86 and PD-L1 on splenic DCs (Fig. 5f and Extended Data Fig. 9f). In the context of infection, anti-CD40 treatment rescued CD8⁺

T cell proliferation in tumor-burdened animals 7 d after infection (Fig. 5g). We also observed significantly higher levels of activation markers CD80, CD54 and PD-L1 on DCs after treatment (Extended Data Fig. 9e), consistent with enhanced APC stimulation. In contrast, high doses of IL-12 or treatment with anti-CTLA-4 failed to rescue T cell proliferation (Fig. 5g and Extended Data Fig. 9g), suggesting that T cell-targeted interventions alone are not sufficient. These experiments demonstrate that APCs failed to drive optimal new T cell responses in the context of tumor burden.

Tumor resection reverses changes in systemic immune organization and responsiveness. Given that defects in T cell activity were reversed after removal from a tumor-burdened context, we asked whether tumor clearance was sufficient to revert changes in systemic immunity. We surgically resected tumors when systemic



changes were evident across sites and allowed mice to recover from surgery for 14 d to mitigate immune confounders from wound healing. We carefully tracked both local recurrence and metastatic

outgrowth by bioluminescent imaging. Successful tumor resection reversed changes in systemic immunity in the AT3 and 4T1 breast cancer and the MC38 colorectal cancer models (Fig. 6a). Splenic

Fig. 6 | Tumor resection completely resets the systemic immune landscape. **a**, Heat maps of \log_2 fold changes in peripheral immune frequencies from tumor-burdened (T) or resected (R) mice. **b, c**, Scaffold maps of spleen immune frequencies (**b**) and proliferation (**c**) after AT3 resection compared to control ($n=3$ per group). Insets show R compared to T mice ($n=4$), $q < 0.05$ by significance analysis of microarrays. **d, e**, Compositional Aitchison distances in spleen immune frequencies (**d**) or T cell cluster frequencies (**e**) from control ($n=3$ for AT3, 8 for 4T1 and 5 for MC38), tumor-burdened ($n=6$, 8 and 4), resected ($n=3$, 6 and 6) or locally recurrent mice for AT3 and distal lung metastasis for 4T1 ($n=3$ for both) (two independent experiments for 4T1 and one experiment for AT3 and MC38). **f, g**, Quantification and representative scatter plots of splenic CD8⁺ T cell proliferation (**f**) and granzyme B production (**g**) after *Lm* infection in control ($n=4$ and $n=7$), AT3 tumor-burdened ($n=4$), resected ($n=17$) or recurrent ($n=4$) mice, three independent experiments. **h–k**, Compositional Aitchison distances of spleen immune frequencies (**h**), spleen frequencies of neutrophil (top) and undefined CD11b⁺ cells (bottom) (**i**), compositional Aitchison distances of T cell subset frequencies (**j**) and splenic CD8⁺ T cell frequencies (**k**) from control or tumor-burdened mice untreated or with IL-1, G-CSF or TGF- β antibody blockade ($n=5$ per group, from one experiment). For all box plots, center line, median; box limits, upper and lower quartiles; whiskers, $1.58 \times$ interquartile range / \sqrt{n} ; points, outliers. For all bar plots, * $P < 0.05$, ** $P < 0.01$ and *** $P < 0.001$ by two-sided *t*-test; center, mean; whiskers, s.d.

immune cluster frequencies and proliferative behavior became similar to control animals (Fig. 6b,c and Extended Data Fig. 10a–c). Successful resection restored compositional changes in spleen immune frequencies and T cell clusters; however, local recurrence in the AT3 model and overt lung metastasis in the 4T1 model led to intermediate phenotypes in the systemic immune state (Fig. 6d,e and Extended Data Fig. 10d,f,g). Local recurrence induced changes in the spleen similar to primary tumors, but the composition of T cells was less dramatically altered. Lung metastasis induced more moderate changes, suggesting that systemic immune perturbations are not primarily the consequence of disseminated metastases. Finally, we interrogated DC and T cell responses 7 d after *Lm*-OVA infection and observed higher CD86 and PD-L1 expression on DCs in successfully resected mice (Extended Data Fig. 10h), and both T cell proliferation and granzyme B production were restored (Fig. 6f,g). Local recurrence mitigated this rescue. Thus, changes in the immune macroenvironment, unlike those of T cells in the TME, are highly dependent on ongoing tumor burden and are reversible upon effective tumor clearance.

Finally, we investigated circulating cytokine levels to define potential mediators of tumor-driven systemic immune remodeling. We reasoned that candidate factors would be elevated in the serum of AT3 tumor-burdened mice, reduced in successfully resected animals and elevated again with local recurrence or vice versa. We found that levels of the inflammatory cytokines IL-1 α and granulocyte colony-stimulating factor (G-CSF) followed this pattern (Extended Data Fig. 10i). Notably, recent studies have implicated G-CSF as a driver of myeloid-derived suppressor cell and neutrophil expansion in preclinical models and in patients with cancer^{12,37,38}. Although IL-1 β has been shown to promote tumor development locally in the TME, the role of IL-1 α is less well understood, though it is elevated in human breast cancers^{39–41}. Consistent with the hypothesis that tumor-secreted factors contribute to systemic immune remodeling, G-CSF and IL-1 α but not IL-1 β were produced by AT3 cancer cells *in vitro* (Extended Data Fig. 10j). We next treated mice with IL-1 and G-CSF blocking antibodies starting 5 d after tumor initiation, before most systemic immune changes. We also investigated the potential systemic effects of transforming growth factor (TGF)- β , a pleiotropic cytokine known to play key roles in shaping the TME, including immune cell exclusion and immunosuppression^{42,43}. Both IL-1 and G-CSF blockade significantly abrogated systemic immune remodeling, whereas TGF- β blockade had no effect (Fig. 6h and Extended Data Fig. 10e). IL-1 and G-CSF blockade reduced splenic neutrophils and less mature CD11b⁺ myeloid cells (Fig. 6i). Notably, IL-1 blockade also significantly reduced circulating levels of G-CSF, suggesting that IL-1 might act upstream to promote G-CSF production (Extended Data Fig. 10k), consistent with *in vitro* data from human tumor cell lines⁴⁴. IL-1 blockade was additionally sufficient to reduce tumor effects on the splenic T cell composition, preventing the observed reductions in naïve and central memory CD8 T cells (Fig. 6j,k). Thus, circulating IL-1 α and G-CSF

are critical mediators of tumor-driven systemic immune remodeling in this context.

Discussion

In this study, we constructed a comprehensive landscape of the immune macroenvironment in cancer, revealing a systemic immune context to consider when targeting immune behavior therapeutically. Strong preexisting T cell activity is associated with clinical benefit from currently available immunotherapies, but many patients with cancer likely require the priming of new anti-tumor immune responses. However, the ability of a tumor-burdened immune system to establish new responses is poorly defined^{45–47}. Patients with cancer are more susceptible to opportunistic infections and mount less effective responses to vaccines^{48,49}, although the relative contributions of tumor-driven systemic disruption and cytotoxic cancer therapies are debated. Here we showed that systemic immunity was disrupted to varying degrees across tumor types. Systemic immune alterations in breast cancer impaired new immune responses, even to highly immunogenic pathogens that do not share tumor antigens. This challenges the idea that T cell dysfunction in cancer is limited to tumor-specific T cells experiencing chronic antigen exposure. Our data revealed impairment in the initial coordination of a T cell response by APCs, affecting T cell proliferation and differentiation. Impaired type 1 immune responses represent a fundamental, but previously unappreciated, obstacle for effective immunotherapy. These results, along with promising clinical results of CD40 agonism in pancreatic cancer⁵⁰, strongly support combinatorial therapeutic strategies that include APC activation.

This work further revealed remarkable plasticity in the systemic immune state, as successful tumor resection largely reverted systemic immune disruptions. Influenced by physiological context, immunotherapies might have different consequences when applied pre- or post-operatively. These studies show that the immune macroenvironment in cancer is highly manipulatable, warranting further studies in patients with cancer. Prior studies connected systemic changes with relapse in patients with breast cancer, showing altered immune gene signatures in uninvolved lymph nodes and blood of patients with metastatic versus non-metastatic disease⁵¹ and that circulating CD45RA⁺Foxp3^{high} Tregs predict future relapse⁵². In breast tumor models, we showed that the primary tumor is a primary driver of systemic immune reorganization but that lung and lymph node metastasis are also associated with additional subtle changes. Future work to understand systemic immune alterations across patients with cancer could inform prognosis and optimal therapy.

Our study lays the foundation for detailed studies of specific tumor macroenvironments to match our detailed understanding of TMEs in mouse tumor models and patients. Building a complete understanding of systems-level immunity in cancer should further our ability to drive effective and rationally designed anti-tumor immune responses in all patients with cancer.

Online content

Any methods, additional references, Nature Research reporting summaries, source data, extended data, supplementary information, acknowledgements, peer review information; details of author contributions and competing interests; and statements of data and code availability are available at <https://doi.org/10.1038/s41591-020-0892-6>.

Received: 30 September 2019; Accepted: 17 April 2020;

Published online: 25 May 2020

References

- Philip, M. et al. Chromatin states define tumour-specific T cell dysfunction and reprogramming. *Nature* **545**, 452–456 (2017).
- Spitzer, M. H. et al. Systemic immunity is required for effective cancer immunotherapy. *Cell* **168**, 487–502 (2017).
- Fransen, M. F. et al. Tumor-draining lymph nodes are pivotal in PD-1/PD-L1 checkpoint therapy. *JCI Insight* **3**, 1–7 (2018).
- Tang, H. et al. PD-L1 on host cells is essential for PD-L1 blockade-mediated tumor regression. *J. Clin. Invest.* **128**, 580–588 (2018).
- Chamoto, K. et al. Mitochondrial activation chemicals synergize with surface receptor PD-1 blockade for T cell-dependent antitumor activity. *PNAS* **114**, E761–E770 (2017).
- Mathios, D. et al. Anti-PD-1 antitumor immunity is enhanced by local and abrogated by systemic chemotherapy in GBM. *Sci. Transl. Med.* **8**, 370ra180 (2016).
- Lin, H. et al. Host expression of PD-L1 determines efficacy of PD-L1 pathway blockade-mediated tumor regression. *J. Clin. Invest.* **128**, 805–815 (2018).
- Curiel, T. J. et al. Blockade of B7-H1 improves myeloid dendritic cell-mediated antitumor immunity. *Nat. Med.* **9**, 562–567 (2003).
- Yost, K. E. et al. Clonal replacement of tumor-specific T cells following PD-1 blockade. *Nat. Med.* **25**, 1251–1259 (2019).
- McAllister, S. S. & Weinberg, R. A. The tumour-induced systemic environment as a critical regulator of cancer progression and metastasis. *Nat. Cell Biol.* **16**, 717–727 (2014).
- Zhang, S. et al. The role of myeloid-derived suppressor cells in patients with solid tumors: a meta-analysis. *PLoS ONE* **11**, e0164514 (2016).
- Casbon, A.-J. et al. Invasive breast cancer reprograms early myeloid differentiation in the bone marrow to generate immunosuppressive neutrophils. *Proc. Natl Acad. Sci. USA* **112**, E566–E575 (2015).
- Meyer, M. A. et al. Breast and pancreatic cancer interrupt IRF8-dependent dendrite cell development to overcome immune surveillance. *Nat. Commun.* **9**, 1–19 (2018).
- Barnstorf, I. et al. Chronic virus infection compromises memory bystander T cell function in an IL-6/STAT1-dependent manner. *J. Exp. Med.* **216**, 571–586 (2019).
- Snell, L. M. et al. CD8⁺ T cell priming in established chronic viral infection preferentially directs differentiation of memory-like cells for sustained immunity. *Immunity* **49**, 678–694 (2018).
- Osborne, L. C. et al. Virus-helminth coinfection reveals a microbiota-independent mechanism of immunomodulation. *Science* **345**, 578–582 (2014).
- Danna, E. A. et al. Surgical removal of primary tumor reverses tumor-induced immunosuppression despite the presence of metastatic disease. *Cancer Res.* **64**, 2205–2211 (2004).
- Ghochikyan, A. et al. Primary 4T1 tumor resection provides critical ‘window of opportunity’ for immunotherapy. *Clin. Exp. Metastasis* **31**, 185–198 (2014).
- Mosely, S. I. S. et al. Rational selection of syngeneic preclinical tumor models for immunotherapeutic drug discovery. *Cancer Immunol. Res.* **5**, 29–41 (2017).
- Westcott, P. M. K. et al. The mutational landscapes of genetic and chemical models of Kras-driven lung cancer. *Nature* **517**, 489–492 (2015).
- Zeitouni, B. et al. Abstract 1840: Whole-exome somatic mutation analysis of mouse cancer models and implications for preclinical immunomodulatory drug development. In *Proceedings of the 107th Annual Meeting of the American Association for Cancer Research* <https://doi.org/10.1158/1538-7445.AM2017-1840> (AACR, 2017).
- Heinzel, F. P., Sadick, M. D., Holaday, B. J., Coffman, R. L. & Locksley, R. M. Reciprocal expression of interferon γ or interleukin 4 during the resolution or progression of murine leishmaniasis. Evidence for expansion of distinct helper T cell subsets. *J. Exp. Med.* **169**, 59–72 (1989).
- Kather, J. N. et al. Topography of cancer-associated immune cells in human solid tumors. *eLife* **7**, e36967 (2018).
- Spitzer, M. H. et al. An interactive reference framework for modeling a dynamic immune system. *Science* **349**, 1259425 (2015).
- Anz, D. et al. CD103 is a hallmark of tumor-infiltrating regulatory T cells. *Int. J. Cancer* **129**, 2417–2426 (2011).
- Ross, E. A. et al. CD31 is required on CD4⁺ T cells to promote T cell survival during *Salmonella* infection. *J. Immunol.* **187**, 1553–1565 (2011).
- Hänninen, A., Maksimow, M., Alam, C., Morgan, D. J. & Jalkanen, S. Ly6C supports preferential homing of central memory CD8⁺ T cells into lymph nodes. *Eur. J. Immunol.* **41**, 634–644 (2011).
- Fourcade, J. et al. Upregulation of Tim-3 and PD-1 expression is associated with tumor antigen-specific CD8⁺ T cell dysfunction in melanoma patients. *J. Exp. Med.* **207**, 2175–2186 (2010).
- Mita, Y. et al. Crucial role of CD69 in anti-tumor immunity through regulating the exhaustion of tumor-infiltrating T cells. *Int. Immunol.* **30**, 559–567 (2018).
- Sun, C., Mezzadra, R. & Schumacher, T. N. Regulation and function of the PD-L1 checkpoint. *Immunity* **48**, 434–452 (2018).
- Bianchini, M. et al. PD-L1 expression on nonclassical monocytes reveals their origin and immunoregulatory function. *Sci. Immunol.* **4**, eaar3054 (2019).
- Busch, D. H., Pilip, I. M., Vlijh, S. & Pamer, E. G. Coordinate regulation of complex T cell populations responding to bacterial infection. *Immunity* **8**, 353–362 (1998).
- Kaech, S. M. & Ahmed, R. Memory CD8⁺ T cell differentiation: initial antigen encounter triggers a developmental program in naïve cells. *Nat. Immunol.* **2**, 415–422 (2001).
- Herndler-Brandstetter, D. et al. KLRLG1⁺ effector CD8⁺ T cells lose KLRLG1, differentiate into all memory T cell lineages, and convey enhanced protective immunity. *Immunity* **48**, 716–729 (2018).
- Jung, S. et al. In vivo depletion of CD11c⁺ dendritic cells abrogates priming of CD8⁺ T cells by exogenous cell-associated antigens. *Immunity* **17**, 211–220 (2002).
- Gabrilovich, D. I., Corak, J., Ciernik, I. F., Kavanaugh, D. & Carbone, D. P. Decreased antigen presentation by dendritic cells in patients with breast cancer. *Clin. Cancer Res.* **3**, 483–490 (1997).
- Coffelt, S. B. et al. IL-17-producing $\gamma\delta$ T cells and neutrophils conspire to promote breast cancer metastasis. *Nature* **522**, 345–348 (2015).
- Wu, W.-C. et al. Circulating hematopoietic stem and progenitor cells are myeloid-biased in cancer patients. *Proc. Natl Acad. Sci. USA* **111**, 4221–4226 (2014).
- Apte, R. N. et al. Effects of micro-environment- and malignant cell-derived interleukin-1 in carcinogenesis, tumour invasiveness and tumour-host interactions. *Eur. J. Cancer* **42**, 751–759 (2006).
- Wu, T. C. et al. IL1 receptor antagonist controls transcriptional signature of inflammation in patients with metastatic breast cancer. *Cancer Res.* **78**, 5243–5258 (2018).
- Singer, C. F. et al. Interleukin-1 α protein secretion in breast cancer is associated with poor differentiation and estrogen receptor α negativity. *Int. J. Gynecol. Cancer* **16**, 556–559 (2006).
- Pickup, M., Novitskiy, S. & Moses, H. L. The roles of TGF β in the tumour microenvironment. *Nat. Rev. Cancer* **13**, 788–799 (2013).
- Mariathasan, S. et al. TGF β attenuates tumour response to PD-L1 blockade by contributing to exclusion of T cells. *Nature* **554**, 544–548 (2018).
- Suzuki, A. et al. IL-1 production as a regulator of G-CSF and IL-6 production in CSF-producing cell lines. *Br. J. Cancer* **65**, 515–518 (1992).
- Mittal, R., Wagener, M., Breed, E. R., Liang, Z. & Yoseph, B. P. Phenotypic T cell exhaustion in a murine model of bacterial infection in the setting of pre-existing malignancy. *PLoS ONE* **9**, e93523 (2014).
- Xie, J. et al. Pre-existing malignancy results in increased prevalence of distinct populations of CD4⁺ T cells during sepsis. *PLoS ONE* **13**, e0191065 (2018).
- Russ, A. J. et al. Melanoma-induced suppression of tumor antigen-specific T cell expansion is comparable to suppression of global T cell expansion. *Cell. Immunol.* **271**, 104–109 (2011).
- Klastersky, J. & Aoun, M. Opportunistic infections in patients with cancer. *Ann. Oncol.* **15**, iv329–iv335 (2004).
- Baluch, A. & Pasikhova, Y. Influenza vaccination in oncology patients. *Curr. Infect. Dis. Rep.* **15**, 486–490 (2013).
- O’Hara, M. H. et al. Abstract CT004: A Phase Ib study of CD40 agonistic monoclonal antibody APX005M together with gemcitabine (Gem) and nab-paclitaxel (NP) with or without nivolumab (Nivo) in untreated metastatic ductal pancreatic adenocarcinoma (PDAC) patients. *Clin. Trials* <https://doi.org/10.1158/1538-7445.am2019-ct004> (2019).
- Zuckerman, N. S. et al. Altered local and systemic immune profiles underlie lymph node metastasis in breast cancer patients. *Int. J. Cancer* **132**, 2537–2547 (2012).
- Wang, L. et al. Connecting blood and intratumoral Treg cell activity in predicting future relapse in breast cancer. *Nat. Immunol.* **20**, 1220–1230 (2019).

Publisher’s note Springer Nature remains neutral with regard to jurisdictional claims in published maps and institutional affiliations.

© The Author(s), under exclusive licence to Springer Nature America, Inc. 2020

Methods

Animals. All mice were housed in an American Association for the Accreditation of Laboratory Animal Care-accredited animal facility and maintained in specific pathogen-free conditions. Animal experiments were approved by and conducted in accordance with Institutional Animal Care & Use Program protocol no. AN157618. Wild-type female BALB/c, C57BL/6 and B6;129 F₁ mice between 8 and 10 weeks old were purchased from Jackson Laboratory and housed at our facility. 4T1 (1×10^5 cells per 100 µl) or AT3 (5×10^5 cells per 100 µl) breast cancer cells (1×10^5 cells per 2 µl) were transplanted into the fourth mammary fat pad. SB28 glioblastoma cells (1×10^5 cells per 2 µl) were transplanted into the right cerebral hemisphere by stereotactic injection. MC38 colon cancer cells (1×10^5 cells per 100 µl), B16-F10 melanoma cancer cells (1×10^5 cells per 100 µl) or LMP pancreatic cancer cells (2×10^5 cells per 100 µl) were transplanted into the subcutaneous region of the flank. Female MMTV-PyMT mice were bred at Stanford University. Tyr⁺:CreER;Braf^{V600E/+};Pten^{lox/lox} mice were purchased from Jackson Laboratory and housed at our facility. Tumors were considered well established when they reached approximately 1 cm³ in volume. TCR transgenic OT-I CD45.1 mice and heterozygous CD45.2/CD45.1 mice were bred at our facility. Animals were housed under standard specific pathogen-free conditions with typical light/dark cycles and standard chow.

Cell lines. 4T1 cells were gifted by Dr. Mary Helen Barcellos-Hoff (University of California, San Francisco (UCSF)). AT3 cells were gifted by Dr. Ross Levine (Memorial Sloan Kettering Cancer Center). For in vivo experiments tracking tumor growth and recurrence after resection, we used 4T1 cells expressing mCherry-luciferase and AT3 cells expressing GFP-luciferase. SB28 cells, derived from a NRasV12;shp53;mPGDF transposon-induced glioma⁵³, were gifted by Dr. Hideho Okada (UCSF). LMP cells, derived from the Kras^{G12D/+};LSL-Trp53^{R172H/+};Pdx-1-Cre model of pancreatic cancer⁵⁴, were gifted by Dr. Edgar Engleman (Stanford University). MC38 cells and B16-F10 cells were gifted by Dr. Jeffrey Bluestone (UCSF). 4T1, MC38, B16 and SB28 cells were cultured in RPMI-1640, and AT3 and LMP cells were cultured in DMEM, all supplemented with 10% fetal calf serum, 2 mM L-glutamine, 100 U ml⁻¹ penicillin and 100 mg ml⁻¹ penicillin-streptomycin.

Infectious agents. *Lm* strain 10403s expressing OVA was originally kindly provided by Shomayeh Sanjabi (UCSF)⁵⁵. *Lm*-OVA stocks frozen at -80 °C were grown overnight at 37 °C in BHI broth supplemented with 5 µg ml⁻¹ erythromycin. Then, overnight cultures were subcultured by diluting into fresh BHI broth supplemented with 5 µg ml⁻¹ erythromycin and grown for 4 h. Bacteria colony-forming unit (CFU) was then quantified by measuring optical density at 600 nm. Bacteria were then diluted to 5×10^4 CFU per 100 µl in sterile phosphate-buffered saline (PBS), and 100 µl was injected per mouse intravenously via the retro-orbital vein.

LCMV was kindly provided by Dr. Jason Cyster (UCSF), and mice were infected with pre-titered and aliquoted stocks stored in PBS at -80 °C and diluted with sterile PBS. Mice were infected with 2×10^5 plaque-forming units by intraperitoneal injection.

Mass cytometry antibodies. All mass cytometry antibodies and concentrations used for analysis can be found in Supplementary Table 1. Primary conjugates of mass cytometry antibodies were prepared using the MaxPAR antibody conjugation kit (Fluidigm) according to the manufacturer's recommended protocol. After labeling, antibodies were diluted in Candor PBS Antibody Stabilization solution (Candor Bioscience) supplemented with 0.02% NaN₃ to between 0.1 and 0.3 mg ml⁻¹ and stored long term at 4 °C. Each antibody clone and lot was titrated to optimal staining concentrations using primary murine samples.

Cell preparation. All tissue preparations were performed simultaneously from each individual mouse, as previously reported³. After euthanasia by CO₂ inhalation, peripheral blood was collected via the posterior vena cava before perfusion of the animal and transferred into sodium heparin-coated vacuum tubes before dilution in PBS with 5 mM ethylenediaminetetraacetic acid (EDTA) and 0.5% bovine serum albumin (BSA) (PBS/EDTA/BSA). Spleens and lymph nodes were homogenized in PBS/EDTA at 4 °C. Bone marrow was flushed from the femur and re-suspended in PBS/EDTA at 4 °C. Tumors were finely minced and digested in RPMI-1640 with 4 mg ml⁻¹ collagenase IV and 0.1 mg ml⁻¹ DNase I. After digestion, re-suspended cells were quenched with PBS/EDTA at 4 °C. All tissues were washed with PBS/EDTA and re-suspended 1:1 with PBS/EDTA and 100 nM cisplatin (Enzo Life Sciences) for 60 s before quenching 1:1 with PBS/EDTA/BSA to determine viability as previously described²⁴. Cells were centrifuged at 500g for 5 min at 4 °C and re-suspended in PBS/EDTA/BSA at a density between 1×10^6 and 10×10^6 cells per ml. Suspensions were fixed for 10 min at room temperature using 1.6% paraformaldehyde (PFA) and frozen at -80 °C.

Mass-tag cellular barcoding. Mass-tag cellular barcoding was performed as previously described⁵⁶. Briefly, 1×10^6 cells from each animal were barcoded with distinct combinations of stable Pd isotopes in 0.02% saponin in PBS. Samples from

any given tissue from each mouse per experiment group were barcoded together. Cells were washed once with cell-staining media (PBS with 0.5% BSA and 0.02% NaN₃) and once with 1× PBS and pooled into a single fluorescence-activated cell sorting (FACS) tube (BD Biosciences). After data collection, each condition was deconvoluted using a single-cell debarcoding algorithm⁵⁶.

Mass cytometry staining and measurement. Cells were resuspended in cell-staining media (PBS with 0.5% BSA and 0.02% NaN₃), and metal-labeled antibodies against CD16 and CD32 were added at 20 mg ml⁻¹ for 5 min at room temperature on a shaker to block Fc receptors. Surface marker antibodies were then added, yielding 500-µl final reaction volumes and stained for 30 min at room temperature on a shaker. After staining, cells were washed two times with cell-staining media and then permeabilized with methanol for 10 min at 4 °C. Cells were then washed twice in cell-staining media to remove remaining methanol and stained with intracellular antibodies in 500 ml for 30 min at room temperature on a shaker. Cells were washed twice in cell-staining media and then stained with 1 ml of 1:4,000 191/193Ir DNA intercalator (Fluidigm) diluted in PBS with 1.6% PFA overnight. Cells were then washed once with cell-staining media and then two times with double-deionized (dd) water. Care was taken to assure that buffers preceding analysis were not contaminated with metals in the mass range above 100 Da. Mass cytometry samples were diluted in dd water containing bead standards (see below) to approximately 10^6 cells per ml and then analyzed on a CyTOF 2 mass cytometer (Fluidigm) equilibrated with dd water. We analyzed $1-5 \times 10^6$ cells per animal, per tissue, per timepoint, consistent with generally accepted practices in the field.

Mass cytometry bead standard data normalization. Data normalization was performed as previously described². Briefly, just before analysis, the stained and intercalated cell pellet was resuspended in freshly prepared dd water containing the bead standard at a concentration ranging between 1×10^4 and 2×10^4 beads per ml. The mixture of beads and cells was filtered through filter cap FACS tubes (BD Biosciences) before analysis. All mass cytometry files were normalized together using the mass cytometry data normalization algorithm⁵⁷, which uses the intensity values of a sliding window of these bead standards to correct for instrument fluctuations over time and between samples.

Mass cytometry gating strategy. After normalization and de-barcoding of files, singlets were gated by Event Length and DNA. Live cells were identified by cisplatin-negative cells. All positive and negative populations and antibody-staining concentrations were determined by titration on positive and negative control cell populations.

Scaffold map generation. Statistical scaffold maps were generated using the open source Statistical Scaffold R package available at <https://github.com/SpitzerLab/statisticalScaffold> with modifications detailed below.

Statistical scaffold analysis combines unsupervised clustering to identify immune cell subsets with dimensionality reduction using a force-directed graph to visualize the organization of immune cells within a tissue. Regions of the graph are easy to identify owing to the incorporation of canonical immune cell types defined manually as 'landmarks' in the graph. As previously described^{2,24}, cells from each tissue for all animals were clustered together and then deconvolved into their respective samples. Cluster frequencies or the Boolean expression of specific proteins for each cluster were passed into the Significance Analysis of Microarrays algorithm⁵⁸ (using a *q*-value cutoff of 0.05), and the fold change results were reported (rather than the binary significance cutoff as originally implemented in Spitzer et al.²). Cluster frequencies were also correlated with the time from tumor inoculation using Spearman's rank-ordered correlation. All results were tabulated into the Scaffold map files for visualization through the graphical user interface, with coloring modifications to graph the spectrum of fold change or correlation strength. The fold change was log₂ normalized and graphed with an upper and lower limit of a four-fold difference, unless otherwise indicated. Cluster frequencies were calculated as a percent of total live leukocytes or parent immune subset as indicated. The spleen data from the 4T1 model were used to spatialize the initial Scaffold map because all major, mature immune cell populations are present in that tissue.

Cell frequency heat map generation. Specified subsets—that is, T cells and mononuclear phagocytes—were manually gated from each tissue for all animals and clustered together. Cluster frequencies were calculated as a percent of total live nucleated cells within that subset (excluding erythrocytes). T cells were identified as CD3⁺ or CD11b⁻. Mononuclear phagocytes were defined as CD11b⁺, CD19⁻, CD3⁻ or Ly6G⁻. Heat maps of the resulting cluster frequencies were generated in R.

Human gene expression analysis. Whole blood microarray data were generated by the Norwegian Women and Cancer study and are deposited in the European Genome-phenome Archive under accession number EGAS00001001804 as previously reported⁵⁹. PCA of centered and scaled data was performed in R using

the prcomp function. xCell cell type enrichment analysis⁶⁰ was performed in R using the xCell package (<https://github.com/dviraran/xCell>) using a customized list of cell populations known to exist in peripheral whole blood (B cells, basophils, CD4⁺ memory T cells, CD4⁺ naïve T cells, CD4⁺ T cells, CD4⁺ Tcm, CD4⁺ Tem, CD8⁺ naïve T cells, CD8⁺ T cells, CD8⁺ Tcm, CD8⁺ Tem, cDCs, class-switched memory B cells, eosinophils, erythrocytes, megakaryocytes, memory B cells, monocytes, naïve B cells, neutrophils, NK cells, NKT cells, plasmacytoid dendritic cells, plasma cells, platelets, Tgd cells, Th1 cells, Th2 cells and Tregs).

In vitro CD8 T cell differentiation and cytokine production. Mice bearing 21-d AT3 tumors were euthanized and their spleens were harvested and dissociated. CD8 T cells were enriched using the EasySep Streptavidin Negative Selection Kit with the following biotinylated markers: CD11b, MHCII, CD11c, Gr1, B220, CD4, CD44 and Ter119. Isolated CD8 T cells were then stimulated with plate-bound CD3 and suspended in CD28-containing T cell media for 3 d. The cells were then removed from CD3 and CD28 stimulation and rested for 1 d. Cells were then restimulated with PMA and Ionomycin or left unstimulated for 4 h with brefeldin A and analyzed by flow cytometry.

Adoptive T cell transfer. For OT1 and polyclonal adoptive transfers, CD8 T cells were isolated from the spleens of CD45.1 OT1 TCR transgenic or CD45.1/CD45.2 heterozygote wild-type or CD45.1 BoyJ mice by enrichment with the EasySep Streptavidin Negative Selection Kit with the following biotinylated markers: CD11b, MHCII, CD11c, Gr1, B220, CD4 and Ter119. Cells were stained with CFSE or Cell Trace Violet, and 1×10^5 cells were then adoptively transferred into each recipient mouse via the retro-orbital vein.

Quantifying bacterial burden. To quantify bacterial burden, spleens were harvested and dissociated. Cells from each mouse were lysed in 0.5% Triton X-100 in PBS, cells were serially diluted in duplicate and aliquots were then added to BHI agar and incubated overnight at 37 °C. Colonies grown were then counted to quantify bacterial CFU present.

Treatments. For infection studies, in vivo antibody treatments were given intraperitoneally starting on day 0 of *Lm*-OVA infection: 200 µg of agonistic anti-CD40 (FGK4.5, Bio X Cell) on day 0, 225 µg of recombinant IL-12p70 (BioLegend) daily and 200 µg of anti-CTLA-4 (9H10, Bio X Cell) on day 0 and day 3. For cytokine inhibition studies, in vivo antibody treatments were given intraperitoneally starting on day 5 after injection of AT3 cells: 10 µg of blocking anti-GCSF (67604, R&D Systems) daily and 200 µg of both blocking anti-IL-1 α (ALF-161, Bio X Cell) and blocking anti-IL-1R (JAMA-147, Bio X Cell) every 3 d. We observed compensatory elevations in circulating IL-1 α with anti-IL-1 α treatment, so we added anti-IL-1R to ensure sufficient blockade of this pathway.

Tumor resection. Mice bearing 14-d 4T1 tumors or 16- to 21-d AT3 or MC38 tumors (between 350 and 550 mm³) were anesthetized by intraperitoneal injection with a mixture of ketamine and xylazine and titrated to effect with isoflurane from a precision vaporizer. The surgical site was shaved and sterilized with 70% ethanol and 10% povidone iodine. An incision was made subcutaneously at the anterior midline and along the flank of the side with the tumor, using surgical scissors, to reveal the inguinal mammary tumor. The tumor was teased away using forceps, and the surgical wound was closed with wound clips. Wound clips were removed after 7 d. Twenty percent to 30% of AT3- or 4T1-resected mice had tumor recurrence owing to incomplete removal of primary tumors or outgrowth of micrometastases. These mice were separated from successful resection analyses.

Cytokine quantification. For in vivo circulating plasma cytokines, mice were bled via the retro-orbital vein using heparinized capillary tubes. Blood was then centrifuged at 1,000g for 10 min, and the supernatant plasma was removed for analysis. For tissue culture supernatants, cells were grown for 48 h in fresh media and then supernatant was removed and centrifuged at 3000g for 10 min to remove debris. Plasma and tissue culture supernatant samples were sent to Eve Technologies and analyzed using a multiplex cytokine array.

Flow cytometry. All flow cytometry antibodies and concentrations used for analysis can be found in Supplementary Table 3. Cells were stained for viability with Zombie-NIR stain. Cell surface staining was performed in cell-staining media (PBS with 0.5% BSA and 0.02% Na₃N₃) for 15 min at room temperature. Intracellular staining was performed after fixing cells with BioLegend FluoroFix Buffer and permeabilizing cells with BioLegend's Intracellular Staining Perm Wash Buffer. The following anti-mouse antibodies were used: (PE-Dazzle594)—CD3 (clone 17A2), (PacificBlue)—CD4 (clone RM4-5), (BV786)—CD8 (clone 53-6.7), (APC-Cy7)—CD45 (clone 30-F11), (APC)—CD38 (clone 90), (PE)—CD101 (clone Moushi101), (PD1)—PE-Cy7 (clone 29F.1A12), (BV421)—TCR- β (clone H57-597), (PE)—IFN- γ (clone XMG1.2), (BV711)—IL-2 (clone JES6-5H4), (FITC)—TNF- α (clone MP6-XT22), (BV650)—CD8 (clone 53-6.7),

(BV510)—KLRG1 (clone 2F1-KLRG1), (BV421)—CD62L (clone MEL-14), (FITC)—CD45.2 (clone 104), (APC)—CD8 (clone 53-6.7), (PE-Cy7)—MHC I (clone AF6-120.1) and (PE)—CD45.1 (clone A20). All antibodies were purchased from BioLegend, BD Biosciences or Thermo Fisher Scientific. Stained cells were analyzed with a CytoFLEX flow cytometer (Beckman Coulter) or an LSR II flow cytometer (BD Biosciences).

Singlets were gated by FSC-A and FSC-W, as well as by SSC-A and SSC-W. All positive and negative populations were determined by staining on positive and negative control populations.

Quantification and statistical analysis. Comparison of cell frequencies and protein expression in Statistical Scaffold was performed using Significance Analysis of Microarrays as described above and in Bair and Tibshirani⁵⁸. Features with $q < 0.05$ were considered statistically significant. Comparison of bulk cell frequencies was performed using the Wilcoxon rank-sum test with Benjamini-Hochberg correction in R. Analysis of principal components for human gene expression was performed using the two-sided Wilcoxon rank-sum test in R. Analysis of cell correlation with time was performed using Spearman's correlation with Benjamini-Hochberg correction. All comparisons over 4T1 tumor growth were performed in Prism by one-way ANOVA with Tukey's correction. Unless otherwise stated, all other comparisons after infection, treatment or resection were made using two-sided *t*-tests in Prism. All tests with $P < 0.05$ were considered statistically significant. Unless otherwise stated in the figure legends, $n = 3–6$ independent mice were used for each experimental condition.

Reporting Summary. Further information on research design is available in the Nature Research Reporting Summary linked to this article.

Data availability

All mass cytometry data are publicly available at <https://premium.cytobank.org/cytobank/projects/2433/> or by request to the senior author without restrictions.

Code availability

The updated Statistical Scaffold package is available at <https://github.com/SpitzerLab/statisticalScaffold>.

References

53. Kosaka, A., Ohkuri, T., Program, B. T. & Okada, H. Combination of an agonistic anti-CD40 monoclonal antibody and the COX-2 inhibitor celecoxib induces anti-glioma effects by promotion of type-1 immunity in myeloid cells and T-cells. *Cancer Immunol. Immunother.* **63**, 847–857 (2014).
54. Tseng, W. W. et al. Development of an orthotopic model of invasive pancreatic cancer in an immunocompetent murine host. *Clin. Cancer Res.* **16**, 3684–3695 (2010).
55. Kathryn, E. et al. Cutting edge: CD4 and CD8 T cells are intrinsically different in their proliferative responses. *J. Immunol.* **168**, 1528–1532 (2002).
56. Zunder, E. R. et al. Palladium-based mass-tag cell barcoding with a doublet-filtering scheme and single cell deconvolution algorithm. *Nat. Protoc.* **10**, 316–333 (2015).
57. Finck, R. et al. Normalization of mass cytometry data with bead standards. *Cytometry A* **83**, 483–494 (2013).
58. Bair, E. & Tibshirani, R. Semi-supervised methods to predict patient survival from gene expression data. *PLoS Biol.* **2**, 0511–0522 (2004).
59. Dumeaux, V. et al. Interactions between the tumor and the blood systemic response of breast cancer patients. *PLoS Comput. Biol.* **13**, e1005680 (2017).
60. Aran, D., Hu, Z. & Butte, A. J. xCell: digitally portraying the tissue cellular heterogeneity landscape. *Genome Biol.* **18**, 1–14 (2017).

Acknowledgements

We thank the UCSF Flow Cytometry Core and S. Tamaki for CyTOF maintenance and M.H. Barcellos-Hoff, R. Levine, H. Okada, E. Engleman and J. Bluestone for cell lines, transgenic mice and reagents. We thank L. Lanier, Z. Werb, M.H. Barcellos-Hoff and L. Fong for insightful feedback. This work was supported by National Institutes of Health (NIH) grants DP5OD023056 and P50CA097257 (UCSF Brain Tumor SPORE Developmental Research Program), funds from the UCSF Program for Breakthrough Biomedical Research and investigator funding from the Parker Institute for Cancer Immunotherapy to M.H.S. and by NIH grant S10OD018040, which enabled procurement of the mass cytometer used in this study. This study makes use of data generated by the Norwegian Women and Cancer Study. A full list of investigators who contributed to the generation of the data is available at <http://site.uitt.no/nowac/>. Funding for the project was provided by European Research Council grant ERC-2008-AdG 232997. The Norwegian Women and Cancer Study group is not responsible for the analysis or interpretation of the data presented.

Author contributions

Conceptualization: B.M.A, K.J.H., Y.C. and M.H.S; experimental methodology: B.M.A, K.J.H., C.E.B., A.V., R.D., I.T., D.M.M., N.W.C., Y.C. and M.H.S.; computational methodology: B.M.A. and M.H.S.; investigation: all authors; writing, original draft: B.M.A.; writing, review and editing: all authors; funding acquisition: M.H.S.; supervision: M.H.S.

Competing interests

M.H.S. receives research funding from Roche/Genentech, Bristol-Myers Squibb and Valitor and has been a paid consultant for Five Prime Therapeutics, Ono Pharmaceutical and January Inc.

Additional information

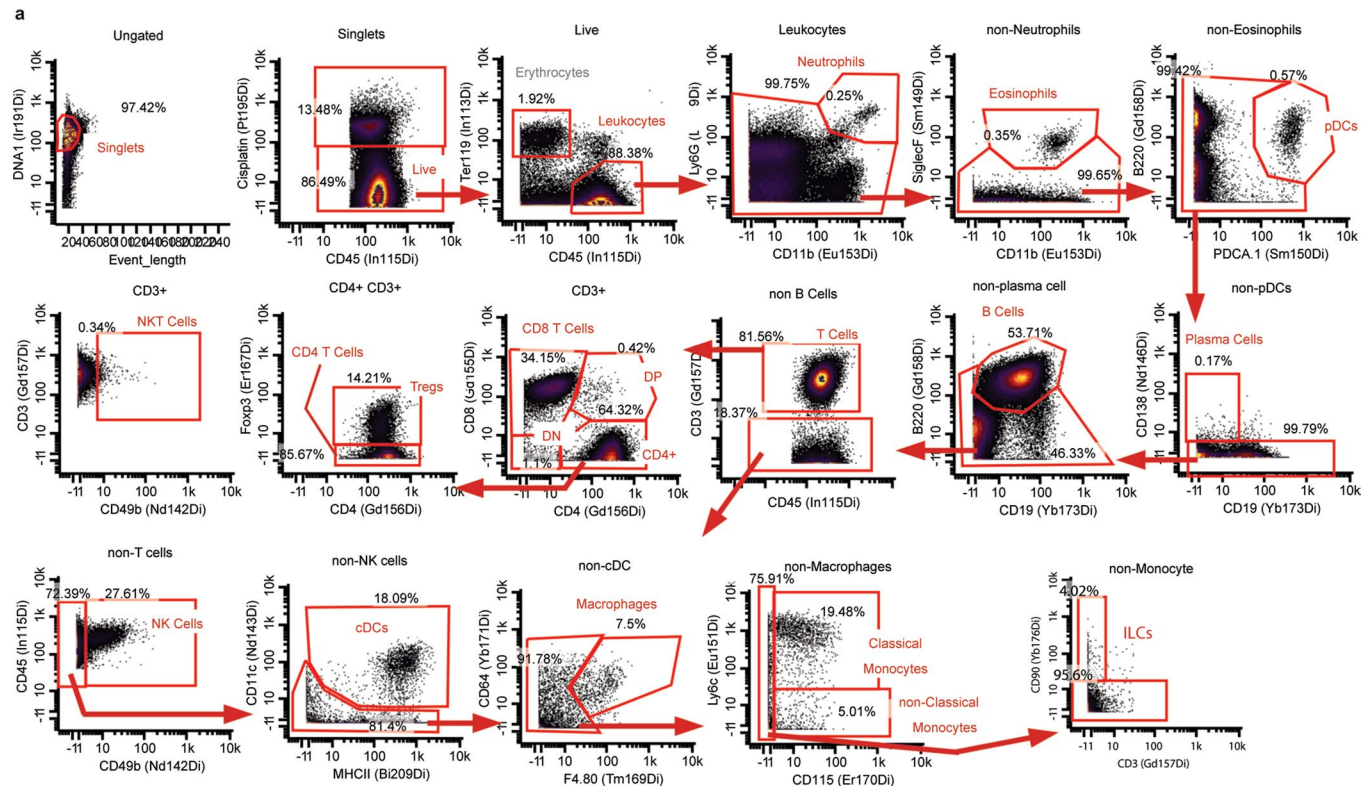
Extended data is available for this paper at <https://doi.org/10.1038/s41591-020-0892-6>.

Supplementary information is available for this paper at <https://doi.org/10.1038/s41591-020-0892-6>.

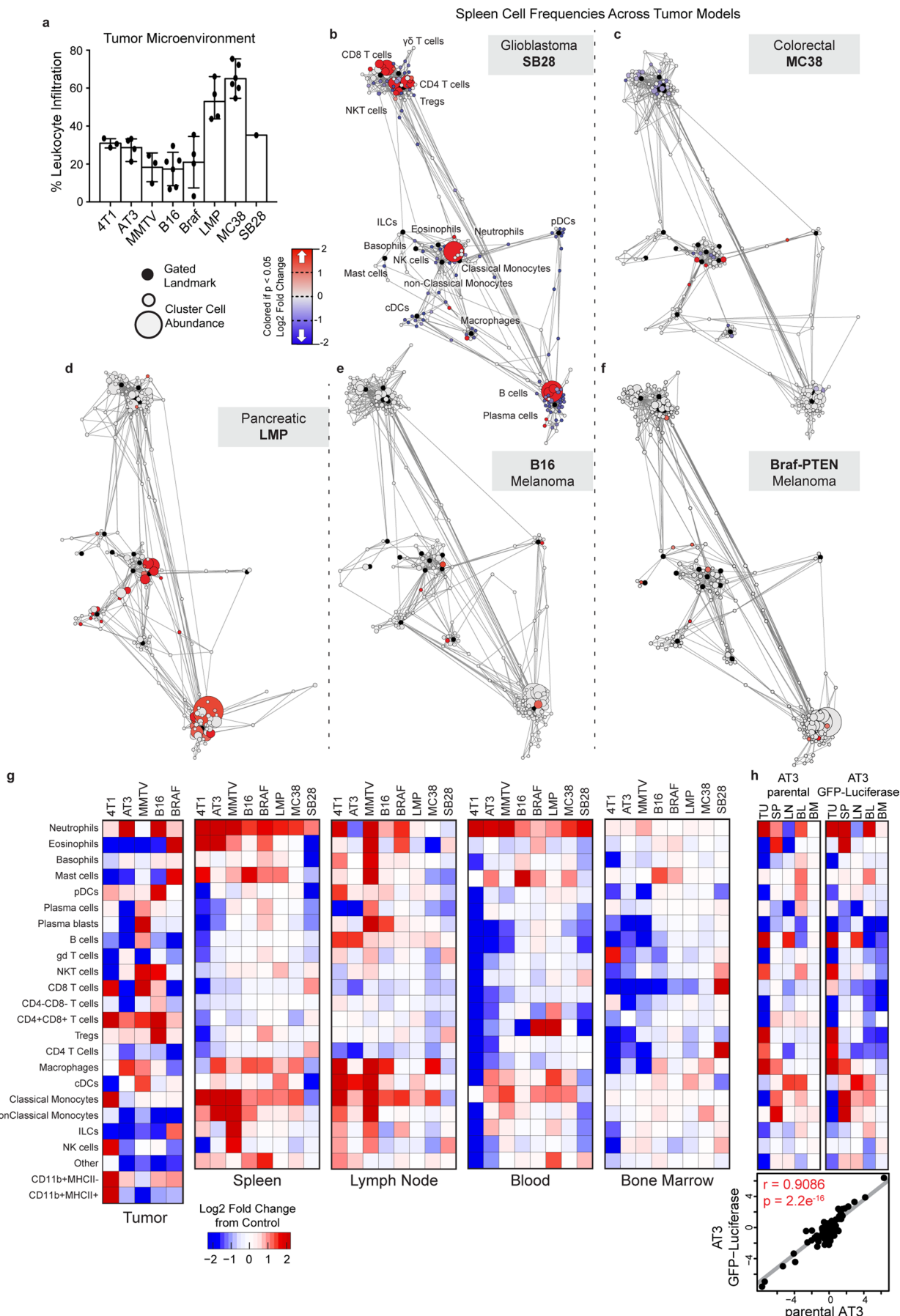
Correspondence and requests for materials should be addressed to M.H.S.

Peer review information Saheli Sadanand was the primary editor on this article and managed its editorial process and peer review in collaboration with the rest of the editorial team.

Reprints and permissions information is available at www.nature.com/reprints.

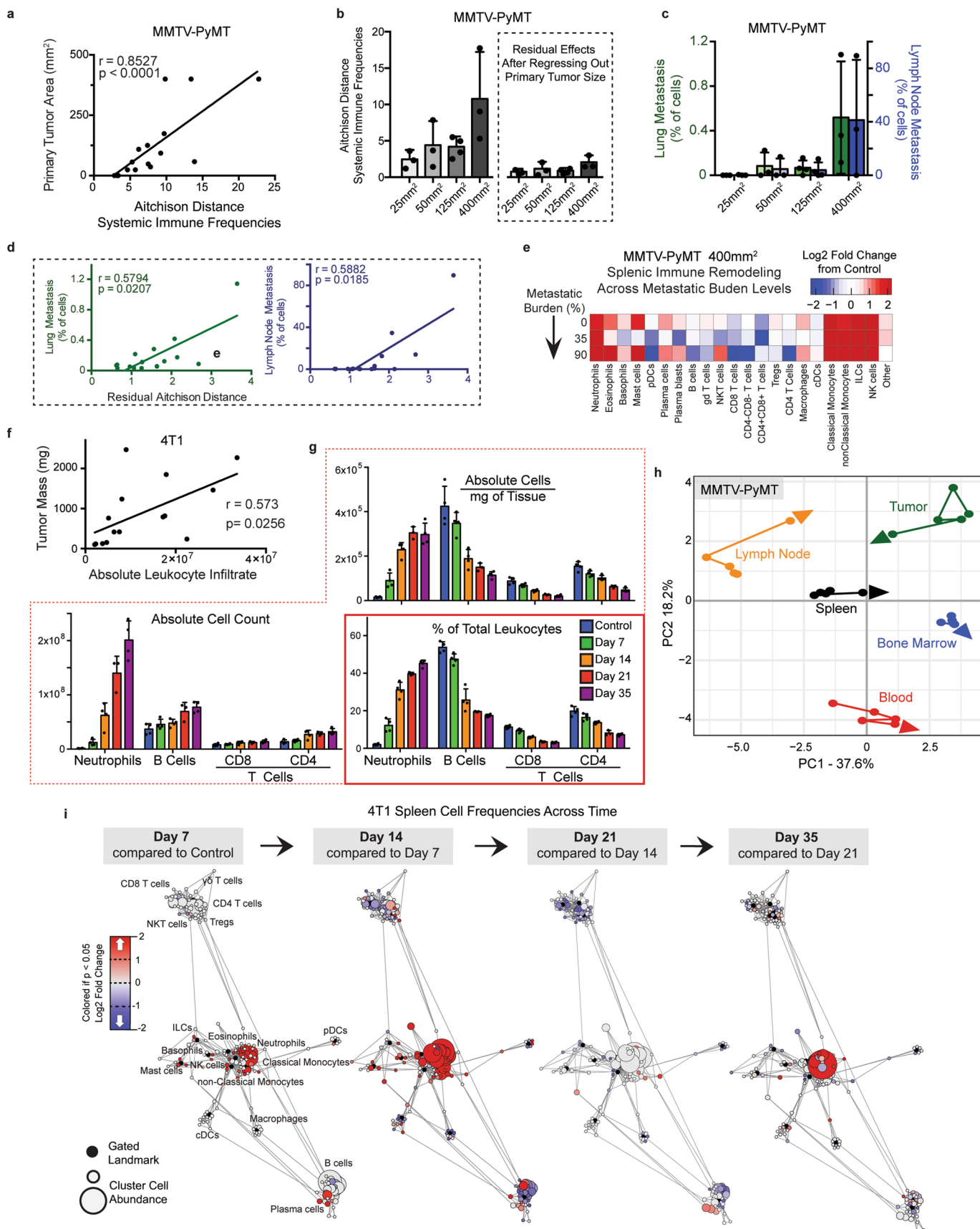


Extended Data Fig. 1 | Main Mass Cytometry Gating Scheme. **a**, Main gating strategy for identifying major immune cell populations from mass cytometry datasets.



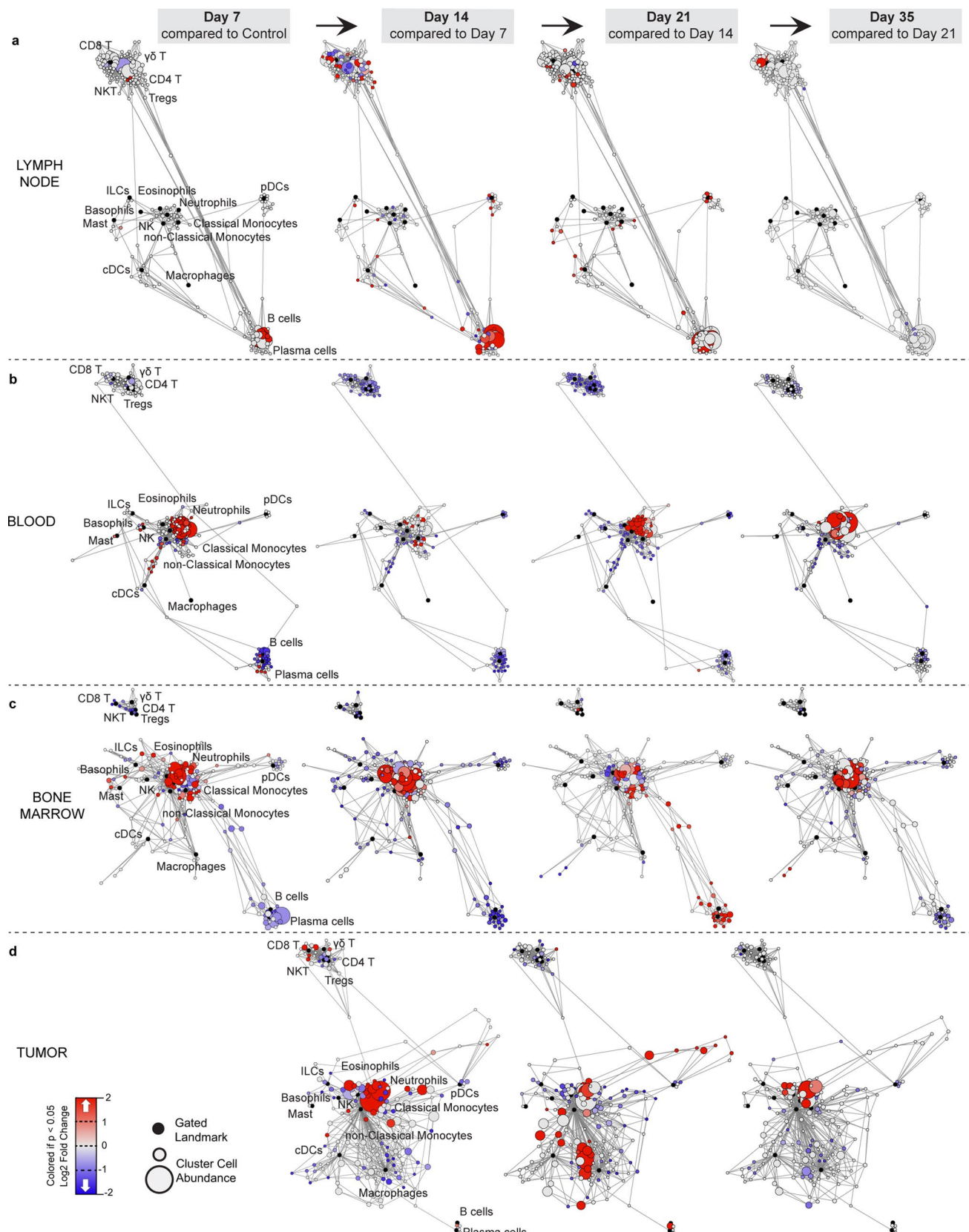
Extended Data Fig. 2 | See next page for caption.

Extended Data Fig. 2 | Systemic immunity is distinctly remodeled across tumor models. **a**, Relative abundance of total leukocytes infiltrating the TME across eight tumor models. **b-f**, Scaffold maps of spleen cell frequencies across five distinct tumor models, SB28 glioblastoma (**b**), MC38 colorectal (**c**), LMP pancreatic (**d**), B16 melanoma (**e**), and Braf/PTEN melanoma (**f**), comparing late stage tumor burden to their respective health littermate controls. **g**, Heatmaps of the log₂ adjusted fold change in bulk immune cell frequencies across all five tissues, where relevant, across all models. **h**, Heatmaps of the log₂ adjusted fold change in bulk immune cell frequencies comparing the parental AT3 and engineered AT3 expressing reporters GFP and Luciferase, with cell labels in g. Lower inset shows Pearson's correlation between these systemic immune features.

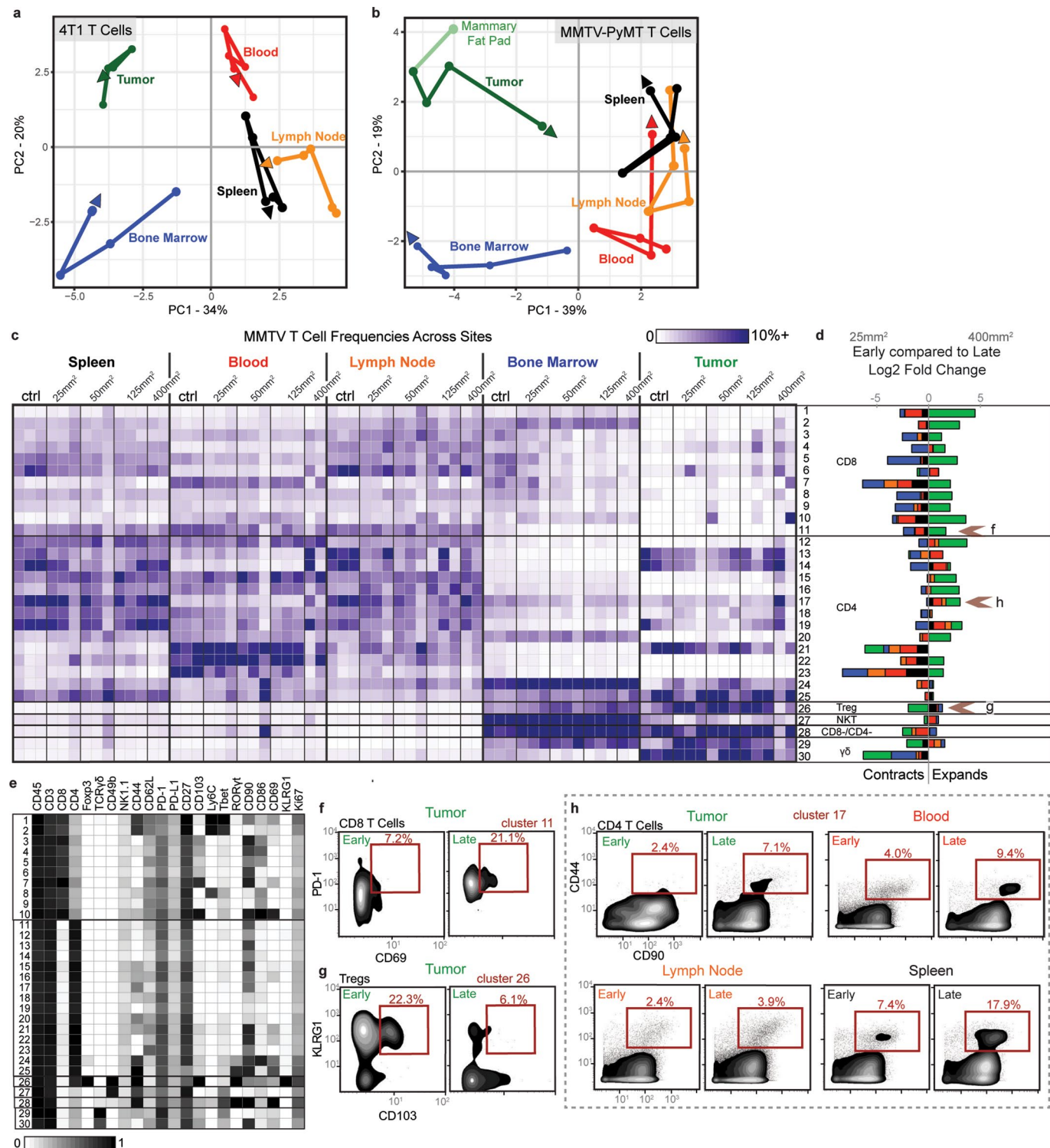


Extended Data Fig. 3 | See next page for caption.

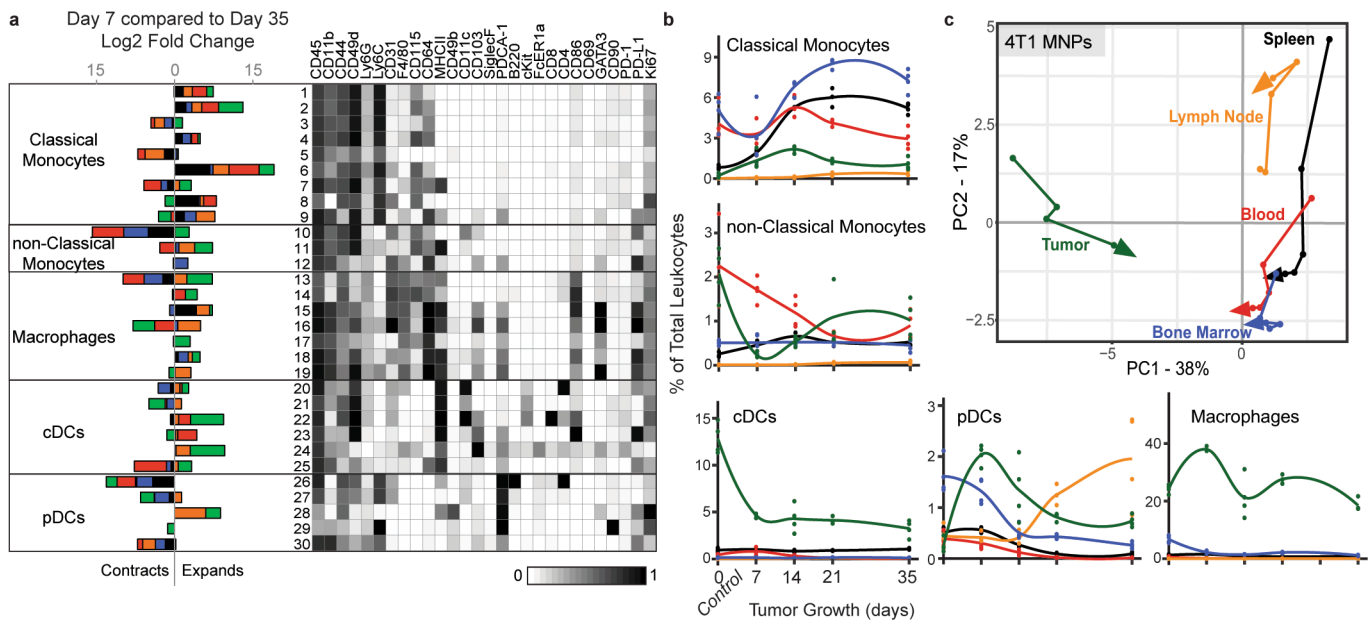
Extended Data Fig. 3 | Systemic immunity is distinctly remodeled over tumor development. **a**, Pearson's correlation between MMTV-PyMT primary tumor size and change in systemic immune composition, measured as Aitchison distance. **b**, Degree of systemic immune change by Aitchison distance over tumor growth (left) and after removing the contribution of primary tumor size by linear regression (right). **c**, Percent of PyMT expressing metastatic cancer cells in the lung (green) and primary draining lymph node (blue). **d**, Pearson's correlation between lung or lymph node metastasis and the residual changes in systemic immune composition after regressing out primary tumor burden. **e**, Heatmap of the log₂ adjusted fold change in bulk spleen immune cell frequencies for each 400mm² tumor-bearing mouse, ranging from 0 to high metastatic disease. **f**, Pearson's correlation between tumor mass and absolute number of infiltrating leukocytes in 4T1 breast tumors. **g**, Spleen immune absolute cell counts, adjusted absolute cell counts per mg of tissue, and unadjusted immune frequencies at each time point for neutrophils, B cells and T cells of the 4T1 breast tumor model. **h**, PCA of relative immune cell frequencies from each major immune tissue over time in the MMTV-PyMT breast tumor model. Vectors designate progression from control (first point) to 25 mm², 50mm², 125mm², and 400mm² (last point, arrowhead). **i**, Scaffold maps of immune cell frequencies in the spleen at each time point of 4T1 tumor burden, colored by log₂ fold change in frequency compared to the previous time point.



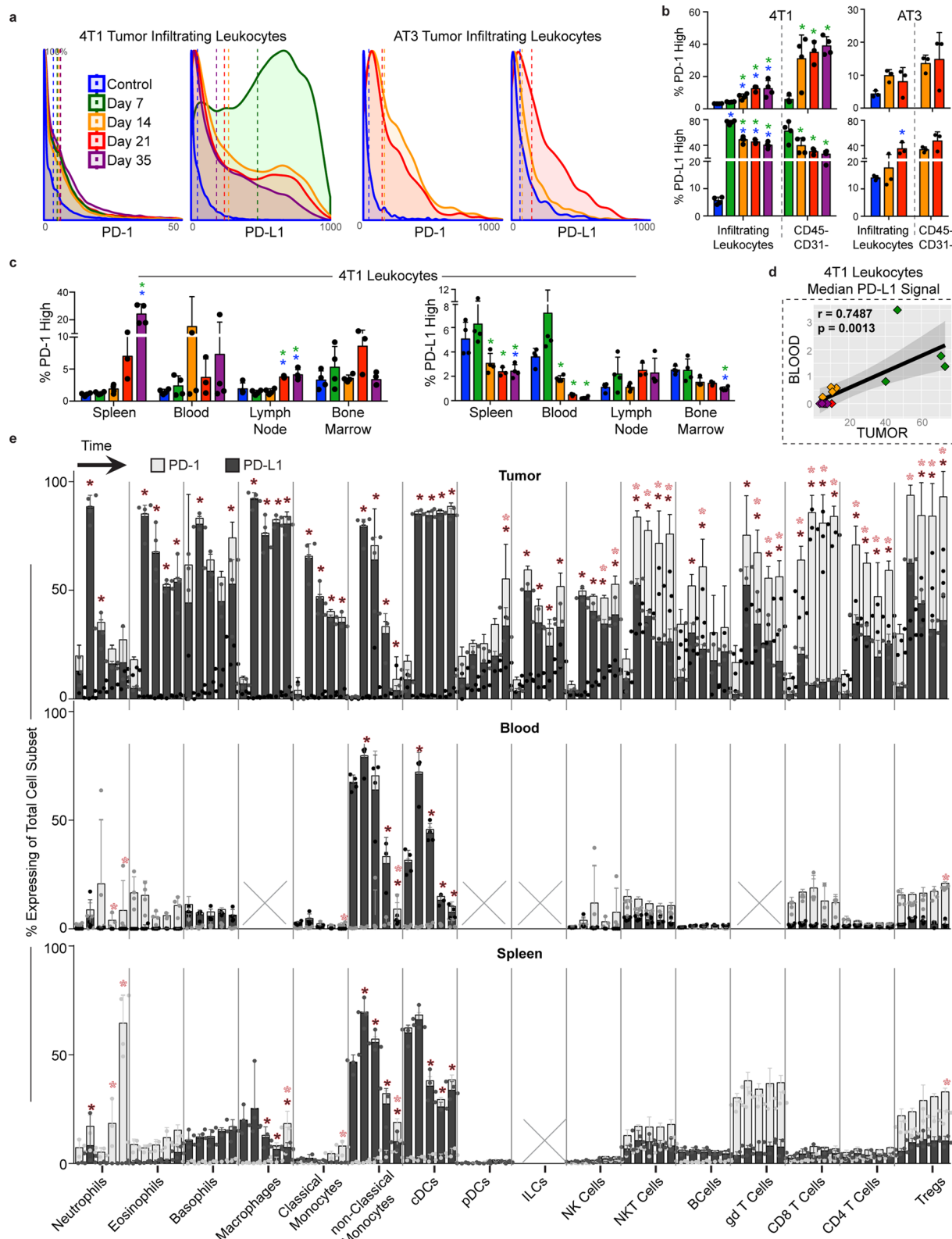
Extended Data Fig. 4 | Immunity is distinctly remodeled by compartment over tumor development. **a-d**, Scaffold maps of immune cell frequencies over 4T1 tumor progression in the tumor draining lymph node (**a**) blood (**b**), bone marrow (**c**), and tumor (**d**), colored by fold change from the previous time point.



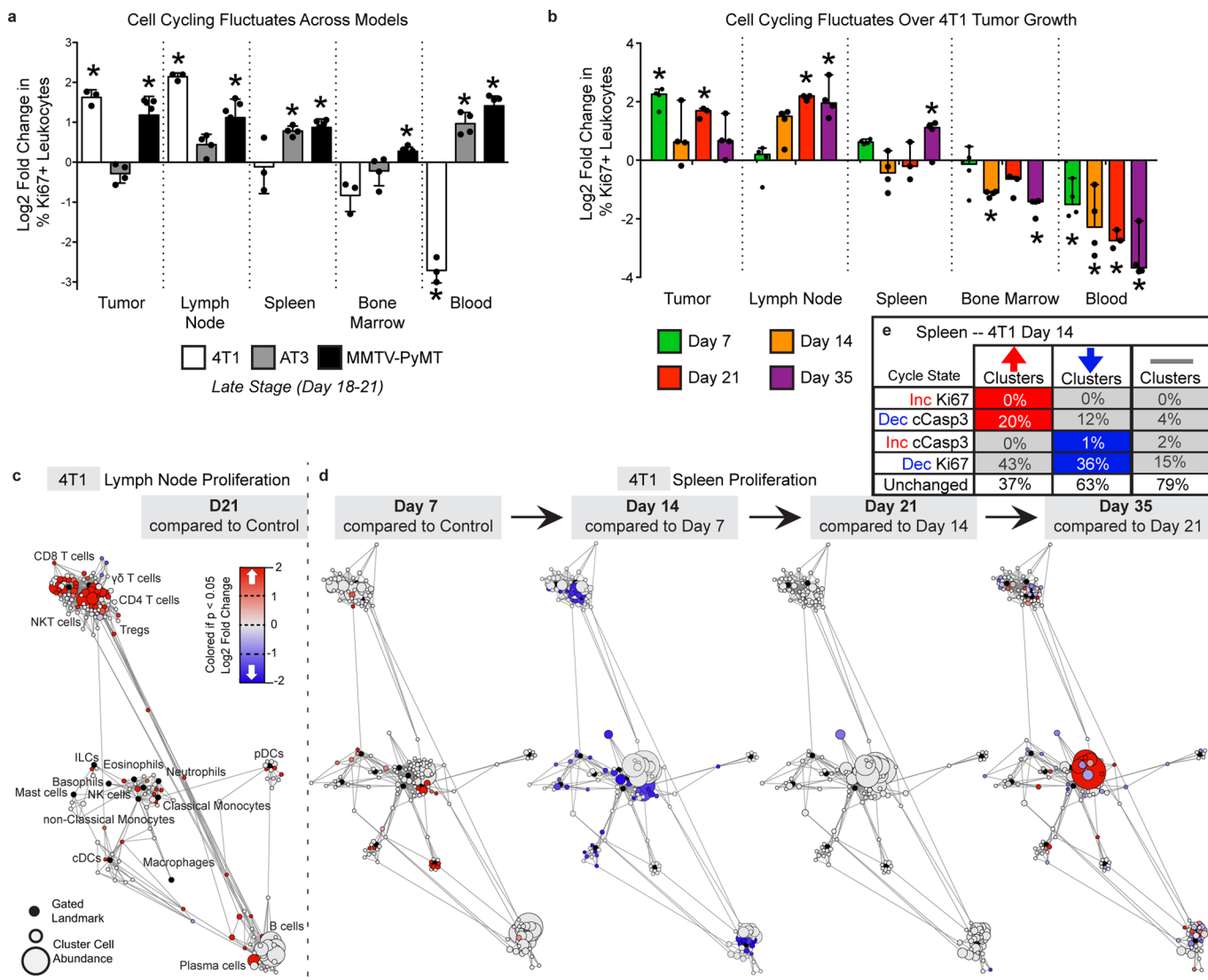
Extended Data Fig. 5 | Tumor growth shifts the systemic T cell composition across models. **a-b**, PCA of T cell cluster frequencies across lymphoid tissues over tumor development for the 4T1 (**a**) and MMTV-PyMT (**b**) breast tumor models. Vectors designate directional progression from control (first point) to late stage disease (last point, arrowhead). In **a**, tumor time points include day 7, 14, 21, and 35 after 4T1 cancer cell transplant. In **b**, tumor time points include tumor sizes of 25 mm², 50 mm², 125 mm², and 400 mm². **c-e**, CD3 + CD11b- leukocytes from all tissues clustered together from healthy and MMTV-PyMT tumor-burdened animals at progressive tumor sizes. **c**, Heatmap of each T cell cluster frequency, by row, in each site and across the individual 2-3 animals per time point. **d**, Stacked bar plot of the log2 fold change in cluster frequency between early (25 mm²) and late (400 mm²) disease time points, colored by tissue. **e**, Heatmap of the protein expression defining each T cell cluster, column normalized to each protein's maximum positive expression. **f-h**, Representative scatter plots of key proteins that define T cell clusters changing in frequency in the designated site between early and late disease stage for CD8 T cells (**f**), Tregs (**g**), and CD4 T Cells (**h**).



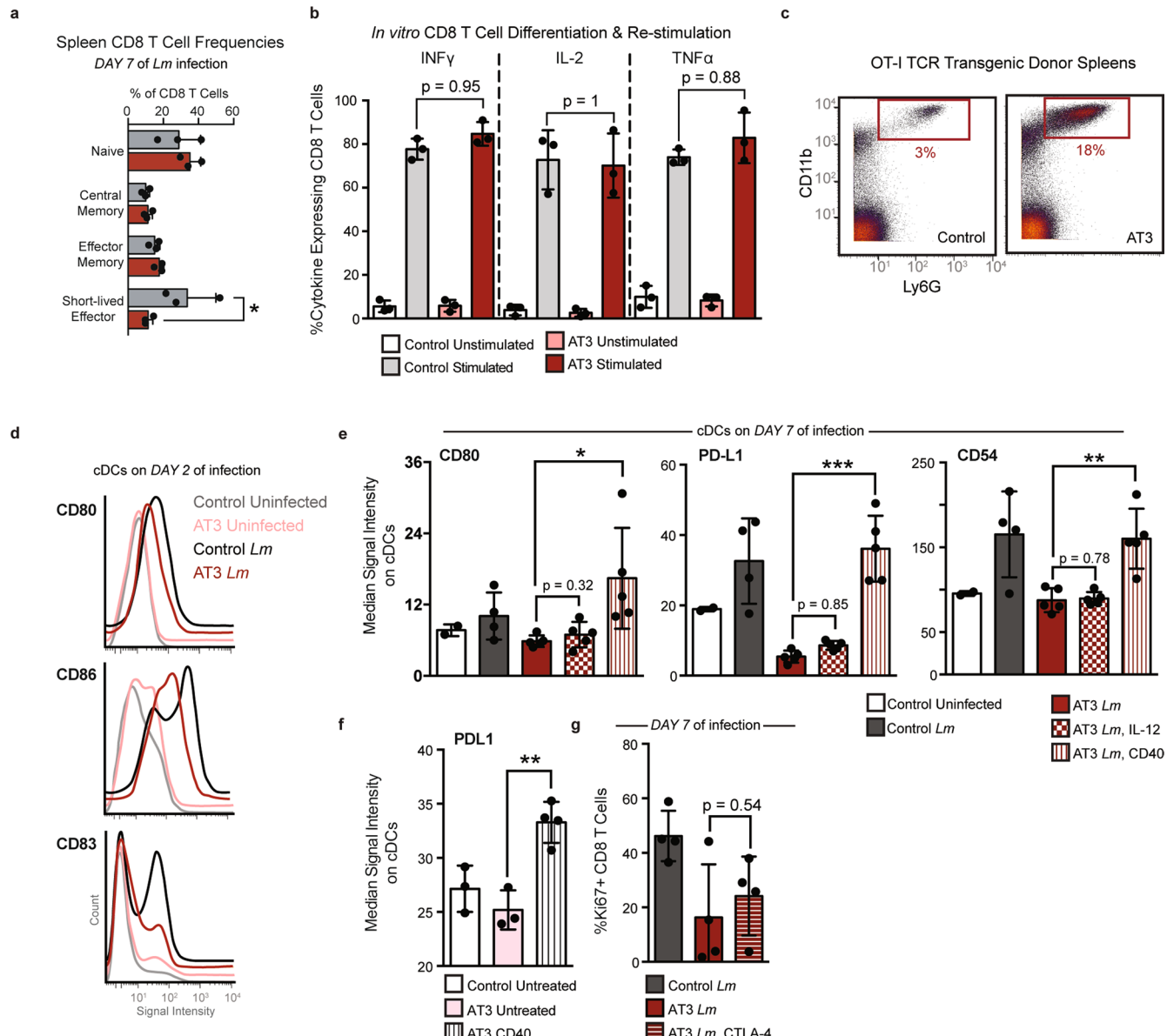
Extended Data Fig. 6 | Tumor growth shifts the systemic mononuclear phagocytic composition. **a**, CD3- CD19- leukocytes from all tissues clustered together from healthy and 4T1 tumor-burdened animals at progressive time points. *Left*, stacked bar plot of the log₂ fold change in cluster frequency between early (day 7) and late (day 35) time points, colored by tissue. *Right*, heatmap of the protein expression defining each cluster, column normalized to each protein's maximum positive expression. **b**, Curves of the mean cell frequencies over time in the 4T1 breast tumor model from designated mononuclear phagocytic cell types, colored by tissue. **c**, PCA of the mononuclear phagocytic cell frequencies from each tissue over time in the 4T1 breast tumor model. Vectors designate progression from control (first point) to day 7, 14, 21, and 35 (last point, arrowhead). Coloring of tissues for a-c corresponds to labels in c.



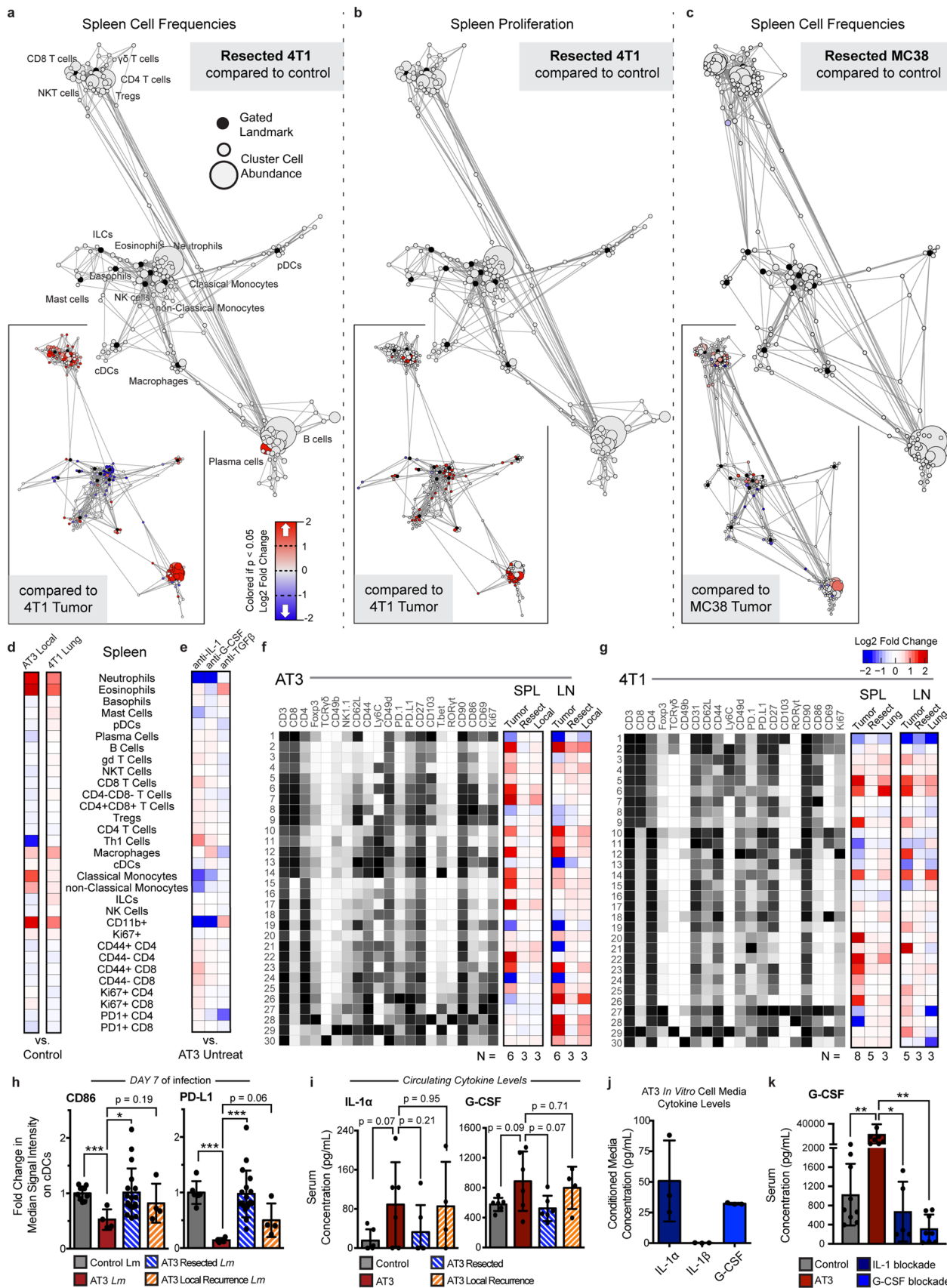
Extended Data Fig. 7 | PD-1 and PD-L1 expression is dynamic over tumor growth. **a**, Distribution of PD-1 and PD-L1 signal intensities on tumor infiltrating leukocytes over time in the 4T1 or AT3 breast tumor models. Coloring of time points for a-d corresponds to legend in a. **b**, Percent of total infiltrating leukocytes (left of dashed line) or CD45⁻, non-endothelial cells (right of dashed line) with high PD-1 or PD-L1 expression in the 4T1 or AT3 tumor models. **c**, Percent of leukocytes with high PD-1 or PD-L1 expression over time and across tissues, 4T1 model. **d**, Pearson's correlation between median PD-L1 signal intensity on blood versus tumor infiltrating leukocytes, 4T1 model. **e**, Percent of each major immune cell subset expressing high PD-1 or PD-L1 in the tumor, blood, and spleen, identified manually. Cell subsets below 0.2% of total leukocytes were not included, X. Bars ordered by time point, beginning at healthy control. Double positive PD-1/PD-L1 expression was rare and not illustrated. $p^* < 0.05$, One-Way ANOVA, with Tukey correction versus control tissue or healthy mammary fat pad (blue in b-c, fill corresponding to bar color in e), or versus day 7 (green in b-c).



Extended Data Fig. 8 | Tumor burden induces tissue-specific changes in immune cell cycling. **a-b**, Log₂ fold change in bulk Ki67 expressing leukocytes in each tissue tissues for 4T1, AT3 and MMTV breast tumors (**a**), and over 4T1 tumor progression (**b**). $p^* < 0.05$, One-Way ANOVA, with Tukey correction versus control. **c-d**, Statistical Scaffold maps of Ki67 expression in immune cells of the tumor draining lymph node comparing control to day 21 (**c**) and the Spleen over time (**d**) in 4T1 tumor burdened animals. **e**, Percent of increasing clusters (red, total of 56), decreasing clusters (blue, total of 90), or unchanged cluster that have corresponding changes in cell cycle markers Ki67 and cleaved Caspase-3.



Extended Data Fig. 9 | Tumor driven deficits in T cell responses are cell-extrinsic. **a**, Quantification of bulk CD8⁺ T cell populations in the spleen of healthy or AT3 tumor-burdened mice after 7 days of *Lm* infection. Two-Way ANOVA with Bonferroni correction. **b**, Expression of inflammatory cytokines, INF γ , IL-2, and TNF α in splenic CD8 T Cells isolated from control or AT3 tumor-burdened mice after *in vitro* differentiation with CD3, CD28 and IL-2, and re-stimulation with BrefeldinA and PMA/Ionomycin. **c**, Scatter plots of CD11b and Ly6G showing expected neutrophilia in OT-I TCR transgenic mice with AT3 tumor burden. **d**, Histograms of CD80, CD86, and CD83 signal intensity on cDCs from healthy or AT3 tumor-burdened mice at day 2 of *Lm*-OVA infection. **e**, Median signal intensity of CD80, PD-L1 and CD54 activation markers on splenic cDCs from healthy or AT3 tumor-burdened mice compared to IL-12p70 or CD40 treatment at day 7 of *Lm*-OVA infection. **f**, Median signal intensity of PD-L1 on splenic cDCs from untreated or CD40 treated AT3 tumor-burdened (day 21) mice. **g**, Quantification of splenic CD8⁺ T cell proliferation in healthy, untreated or CTLA-4 treated AT3 tumor-burdened animals in response to 7 days of *Lm*-OVA infection. p*<0.05, two-tailed t-test.



Extended Data Fig. 10 | See next page for caption.

Extended Data Fig. 10 | Tumor resection resets systemic immune organization and function. **a-c**, Statistical scaffold maps of spleen immune cell frequencies (**a**) and proliferation by Ki67 expression (**b**) in 4T1 resected mice, and of spleen immune cell frequencies in MC38 resected mice (**c**) compared to healthy control. Insets show resected mice compared to tumor-burdened mice. **d-e**, Heatmap of the log₂ fold changes in splenic immune cell frequencies for local or lung recurrences from control mice (**d**), and for IL-1, G-CSF, or TGF β blockade from untreated AT3 tumor-burdened mice (**e**). **f-g**, Heatmaps of T cell cluster expression profiles and log₂ fold change from control for AT3 (**f**) and 4T1 (**g**) for the spleen and draining lymph node. **h**, Median signal intensity of CD86 and PD-L1 on splenic cDCs from healthy, AT3 tumor-burdened, resected, or resected mice with local recurrence at day 7 of *Lm*-OVA infection. **i**, Concentration of circulating cytokines, IL-1 α and G-CSF from healthy, AT3 tumor-burdened, resected, or resected mice with local recurrence. **j**, Concentration of cytokines, IL-1 α , IL-1 β and G-CSF from *in vitro* cell culture media conditioned with AT3 cancer cells. **k**, Concentration of circulating G-CSF from control or AT3 tumor-bearing mice, or AT3 tumor-bearing mice treated with either IL-1 or G-CSF blocking antibodies. $p^*<0.05$, two-tailed t-test.

Reporting Summary

Nature Research wishes to improve the reproducibility of the work that we publish. This form provides structure for consistency and transparency in reporting. For further information on Nature Research policies, see [Authors & Referees](#) and the [Editorial Policy Checklist](#).

Statistics

For all statistical analyses, confirm that the following items are present in the figure legend, table legend, main text, or Methods section.

n/a Confirmed

- The exact sample size (n) for each experimental group/condition, given as a discrete number and unit of measurement
- A statement on whether measurements were taken from distinct samples or whether the same sample was measured repeatedly
- The statistical test(s) used AND whether they are one- or two-sided
Only common tests should be described solely by name; describe more complex techniques in the Methods section.
- A description of all covariates tested
- A description of any assumptions or corrections, such as tests of normality and adjustment for multiple comparisons
- A full description of the statistical parameters including central tendency (e.g. means) or other basic estimates (e.g. regression coefficient) AND variation (e.g. standard deviation) or associated estimates of uncertainty (e.g. confidence intervals)
- For null hypothesis testing, the test statistic (e.g. F , t , r) with confidence intervals, effect sizes, degrees of freedom and P value noted
Give P values as exact values whenever suitable.
- For Bayesian analysis, information on the choice of priors and Markov chain Monte Carlo settings
- For hierarchical and complex designs, identification of the appropriate level for tests and full reporting of outcomes
- Estimates of effect sizes (e.g. Cohen's d , Pearson's r), indicating how they were calculated

Our web collection on [statistics for biologists](#) contains articles on many of the points above.

Software and code

Policy information about [availability of computer code](#)

Data collection

For mass cytometry data collection, we used Fluidigm CyTOF Software version 6.7.1014. For flow cytometry data collection, we used BD FACSDiva version 8.01 and CytExpert version 2.0.0.153.

Data analysis

For analysis of mass cytometry data, we used the publically available Statistical Scaffold package with updates released accompanying this work. For both mass and flow cytometry data analysis and visualizations, we used Cytobank ([cytobank.org](#)) and CellEngine ([cellengine.com](#)). For statistical tests and data visualization, we used Prism version 6.

For manuscripts utilizing custom algorithms or software that are central to the research but not yet described in published literature, software must be made available to editors/reviewers. We strongly encourage code deposition in a community repository (e.g. GitHub). See the Nature Research [guidelines for submitting code & software](#) for further information.

Data

Policy information about [availability of data](#)

All manuscripts must include a [data availability statement](#). This statement should provide the following information, where applicable:

- Accession codes, unique identifiers, or web links for publicly available datasets
- A list of figures that have associated raw data
- A description of any restrictions on data availability

Mass cytometry data will be made publicly available at [www.cytobank.org](#) and at [www.immport.org](#) at the time of publication as we have done for our prior studies.

Field-specific reporting

Please select the one below that is the best fit for your research. If you are not sure, read the appropriate sections before making your selection.

- Life sciences Behavioural & social sciences Ecological, evolutionary & environmental sciences

For a reference copy of the document with all sections, see nature.com/documents/nr-reporting-summary-flat.pdf

Life sciences study design

All studies must disclose on these points even when the disclosure is negative.

Sample size	An N of 3 to 6 mice was used for each condition in each experiment, based on standard practice in the field and prior experience working with the specified mouse models. No explicit power calculation was performed.
Data exclusions	No data were excluded.
Replication	All findings were reproducible, with number of independent experiments detailed in the figure legends.
Randomization	All mice were randomly stratified into groups, with littermates evenly distributed across conditions.
Blinding	No blinding was performed or deemed necessary for these experiments.

Reporting for specific materials, systems and methods

We require information from authors about some types of materials, experimental systems and methods used in many studies. Here, indicate whether each material, system or method listed is relevant to your study. If you are not sure if a list item applies to your research, read the appropriate section before selecting a response.

Materials & experimental systems		Methods	
n/a	Involved in the study	n/a	Involved in the study
<input type="checkbox"/>	<input checked="" type="checkbox"/> Antibodies	<input checked="" type="checkbox"/>	<input type="checkbox"/> ChIP-seq
<input type="checkbox"/>	<input checked="" type="checkbox"/> Eukaryotic cell lines	<input type="checkbox"/>	<input checked="" type="checkbox"/> Flow cytometry
<input checked="" type="checkbox"/>	<input type="checkbox"/> Palaeontology	<input checked="" type="checkbox"/>	<input type="checkbox"/> MRI-based neuroimaging
<input type="checkbox"/>	<input checked="" type="checkbox"/> Animals and other organisms		
<input checked="" type="checkbox"/>	<input type="checkbox"/> Human research participants		
<input checked="" type="checkbox"/>	<input type="checkbox"/> Clinical data		

Antibodies

Antibodies used	Antibodies used: See extended data table 1.
Validation	Validation: All antibodies were individually tested and titrated on relevant positive and negative biological controls.

Eukaryotic cell lines

Policy information about cell lines	
Cell line source(s)	4T1 cells were gifted from Dr. Mary-Helen Barcellos-Hoff (UCSF). AT3 cells were gifted from Dr. Ross Levine (MSKCC). SB28 cells were gifted from Dr. Hideho Okada (UCSF). LMP cells were gifted from Dr. Edgar Engleman (Stanford University). MC38 cells and B16-F10 cells gifted from Dr. Jeffrey Bluestone (UCSF).
Authentication	No additional authentication was performed.
Mycoplasma contamination	All cell lines were tested and found negative for mycoplasma contamination.
Commonly misidentified lines (See ICLAC register)	Name any commonly misidentified cell lines used in the study and provide a rationale for their use.

Animals and other organisms

Policy information about [studies involving animals](#); [ARRIVE guidelines](#) recommended for reporting animal research

Laboratory animals

Animals included wild-type female BALB/c, C57BL/6, and B6;129 F1 mice between 8-10 weeks old; female MMTV-PyMT mice on the FVB background between 6-10 weeks old; Tyr::CreER; BrafV600E+/Ptenlox/lox mice on the C57BL/6 background between 10-13 weeks old ; and female TCR Transgenic OT-I CD45.1 mice and heterozygous CD45.2/CD45.1 mice between 8-10 weeks old.

Wild animals

No wild animals were used in these experiments.

Field-collected samples

No field-collected samples were used in these experiments.

Ethics oversight

All mice were housed in an American Association for the Accreditation of Laboratory Animal Care–accredited animal facility. Animal experiments were approved and conducted in accordance with Institutional Animal Care & Use Program protocol number AN157618.

Note that full information on the approval of the study protocol must also be provided in the manuscript.

Flow Cytometry

Plots

Confirm that:

- The axis labels state the marker and fluorochrome used (e.g. CD4-FITC).
- The axis scales are clearly visible. Include numbers along axes only for bottom left plot of group (a 'group' is an analysis of identical markers).
- All plots are contour plots with outliers or pseudocolor plots.
- A numerical value for number of cells or percentage (with statistics) is provided.

Methodology

Sample preparation

Sample preparation is discussed at length in the methods.

Instrument

Helios CyTOF, Fluidigm; Cytoflex 5, Beckman Coulter; Foretessa X-20, BD.

Software

Fluidigm CyTOF Software version 6.7.1014; CytExpert version 2.0.0.153; BD FACSDiva version 8.01.

Cell population abundance

N/A – no populations were sorted

Gating strategy

Mass Cytometry

After normalization and debarcoding of files, singlets were gated by Event Length and DNA. Live cells were identified by Cisplatin negative cells. Erythrocytes were excluded by gating on Ter119- cells. All positive and negative populations and antibody staining concentrations were determined by titration on positive and negative control cell populations.

Populations were defined as follows.

Neutrophils (CD45+CD11b+Ly6G+)

Eosinophils (CD45+CD11b+SiglecF+)

Mast Cells (CD45+CD11b+Fcer1a+CD49b+SiglecF-Ly6G-)

Basophils (CD45+CD11b+Fcer1a+cKit+SiglecF-Ly6G-)

pDCs (CD45+B220+PDCA1+Ly6G-SiglecF-Fcer1a-)

Plasma cells (CD45+CD138+CD19-Ly6G-SiglecF-Fcer1a-)

B cells (CD45+B220+CD19+CD138-Ly6G-SiglecF-Fcer1a-)

CD8 T cells (CD45+CD3+CD8+TCRgd-NK1.1-B220-CD19-CD138-Ly6G-SiglecF-Fcer1a-)

CD4 T cells (CD45+CD3+CD4+FoxP3-CD8-TCRgd-NK1.1-B220-CD19-CD138-Ly6G-SiglecF-Fcer1a-)

Tregs (CD45+CD3+CD4+FoxP3+CD8-TCRgd-NK1.1-B220-CD19-CD138-Ly6G-SiglecF-Fcer1a-)

gdTCells (CD45+CD3+TCRgd+B220-CD19-CD138-Ly6G-SiglecF-Fcer1a-)

NKT Cells (CD45+CD3+NK1.1+TCRgd-B220-CD19-CD138-Ly6G-SiglecF-Fcer1a-)

NKT Cells, non-Black6 mice (CD45+CD3+CD49b+TCRgd-B220-CD19-CD138-Ly6G-SiglecF-Fcer1a-)

NK Cells (CD45+CD3+NK1.1+CD49b+CD3-CD19-B220-CD138-Ly6G-SiglecF-Fcer1a-)

NK Cells, non-Black6 mice (CD45+CD3+CD49b+CD3-CD19-B220-CD138-Ly6G-SiglecF-Fcer1a-)

Macrophages (CD45+CD64+F480+Ly6G-SiglecF-CD19-B220-CD3-Fcer1a-NK1.1-CD138-)

cDCs (CD45+CD11c+MHCII+CD64-F480-NK1.1-CD3-CD19-B220-CD138-Fcer1a-SiglecF-Ly6G-)

cMonocytes (CD45+CD115+Ly6C+CD11c-CD64-F480-NK1.1-CD3-CD19-B220-CD138-Fcer1a-SiglecF-Ly6G-)

ncMonocytes (CD45+CD115+Ly6C-CD64-F480-NK1.1-CD3-CD19-B220-CD138-Fcer1a-SiglecF-Ly6G-)

ILCs (CD45+CD90+CD115-CD64-F480-NK1.1-CD3-CD19-B220-CD138-Fcer1a-SiglecF-Ly6G-)

Other (CD45+CD115-CD64-F480-NK1.1-CD3-CD19-B220-CD138-Fcer1a-SiglecF-Ly6G-)

Microglia (CD45+CD115high CD64high)

MHC- CD11b high (Lineage Negative Other, MHC- CD11b high)

MHC+ CD11b high (Lineage Negative Other, MHC+ CD11b high)

Plasma Blasts (CD45+CD138+CD19+Ly6G-SiglecF-Fcer1a-)

Th1 cells (CD45+CD3+CD4+FoxP3-Tbet+CD8-TCRgd-NK1.1-B220-CD19-CD138-Ly6G-SiglecF-Fcer1a-)
CD4-CD8- T cells (CD45+CD3+CD4-CD8-TCRgd-NK1.1-B220-CD19-CD138-Ly6G-SiglecF-Fcer1a-)
CD4+CD8+ T cells (CD45+CD3+CD4+CD8+TCRgd-NK1.1-B220-CD19-CD138-Ly6G-SiglecF-Fcer1a-)
Naive CD8 T cells (CD45+CD3+TCRgd-NK1.1-CD8+CD44-CD62L+)
Central Memory CD8 T cells (CD45+CD3+TCRgd-NK1.1-CD8+CD44+CD62L+)
Effector Memory CD8 T cells (CD45+CD3+TCRgd-NK1.1-CD8+CD44+CD62L-)
OT1 T cells (CD45.1+CD45.2-CD3+CD8+)
Polyclonal AT3 tumor experienced CD8 T cells (CD45.1+CD45.2-CD3+CD8+)
Polyclonal healthy CD8 T cells (CD45.1+CD45.2+CD3+CD8+)

Flow Cytometry

All samples were gated for single cells by FSC-W/FSC-A and SSC-W/SSCA. Once single cells were gated, live cells were gated using the Zombie NIR fixable viability dye (BioLegend 423106).

Populations were defined as follows:

CD8 T cells [for CD38 CD101 plot] (CD45+CD3+CD8+)

OT1 Adoptively transferred cells (CD8+CD45.1+)

Healthy Donor OT1 T cells (CD8+CD45.1+CellTraceViolet+CFSE-)

AT3 Tumor Burdened OT1 T cells (CD8+CD45.1+CFSE+CellTraceViolet-)

Tick this box to confirm that a figure exemplifying the gating strategy is provided in the Supplementary Information.